Integrated InSAR monitoring and structural assessment of tunnelling-induced building deformations

Macchiarulo, Valentina; Milillo, Pietro; DeJong, Matthew J.; González Martí, Javier; Sánchez, Jordi; Giardina, Giorgia

DOI
10.1002/stc.2781

Publication date
2021

Document Version
Final published version

Published in
Structural Control and Health Monitoring

Citation (APA)
Macchiarulo, V., Milillo, P., DeJong, M. J., González Martí, J., Sánchez, J., & Giardina, G. (2021). Integrated InSAR monitoring and structural assessment of tunnelling-induced building deformations. *Structural Control and Health Monitoring*, *28*(9), Article e2781. https://doi.org/10.1002/stc.2781

Received: 8 October 2020 | Revised: 9 March 2021 | Accepted: 26 April 2021

DOI: 10.1002/stc.2781

RESEARCH ARTICLE

WILEY

Integrated InSAR monitoring and structural assessment of tunnelling-induced building deformations

Valentina Macchiarulo[1] | **Pietro Milillo**[2] | **Matthew J. DeJong**[3] | **Javier González Martí**[4] | **Jordi Sánchez**[5] | **Giorgia Giardina**[6]

[1]Department of Architecture and Civil Engineering, University of Bath, Bath, UK

[2]Cullen College of Engineering, University of Houston, Houston, Texas, USA

[3]Department of Civil and Environmental Engineering, University of California, Berkeley, California, USA

[4]Sales & Business Development, SAALG Geomechanics, Barcelona, Spain

[5]Post-processing Department, TRE-Altamira, Barcelona, Spain

[6]Department of Geoscience and Engineering, Delft University of Technology, Delft, Netherlands

Correspondence
Giorgia Giardina, Department of Geoscience and Engineering, Delft University of Technology, Delft, Netherlands.
Email: g.giardina@tudelft.nl

Summary

Structural deformation monitoring is crucial for the identification of early signs of tunnelling-induced damage to adjacent structures and for the improvement of current damage assessment procedures. Satellite multi-temporal interferometric synthetic aperture radar (MT-InSAR) techniques enable measurement of building displacements over time with millimetre-scale accuracy. Compared to traditional ground-based monitoring, MT-InSAR can yield denser and cheaper building observations, representing a cost-effective monitoring tool. However, without integrating MT-InSAR techniques and structural assessment, the potential of InSAR monitoring cannot be fully exploited. This integration is particularly demanding for large construction projects, where big datasets need to be processed. In this paper, we present a new automated methodology that integrates MT-InSAR-based building deformations and damage assessment procedures to evaluate settlement-induced damage to buildings adjacent to tunnel excavations. The developed methodology was applied to the buildings along an 8-km segment of the Crossrail tunnel route in London, using COSMO-SkyMed MT-InSAR data from 2011 to 2015. The methodology enabled the identification of damage levels for 858 buildings along the Crossrail twin tunnels, providing an unprecedented number of high quality field observations for building response to settlements. The proposed methodology can be used to improve current damage assessment procedures, for the benefit of future underground excavation projects in urban areas.

KEYWORDS

building damage, damage assessment, MT-InSAR, risk assessment, settlement, soil–structure interaction, structural-health monitoring, tunnelling

1 | INTRODUCTION

Large underground transportation systems reduce traffic, improve air quality and free surface space in urban areas.[1] The development of underground construction projects is supported by multi-billion dollar investments worldwide.[2–5] As an example, the Crossrail project in London, UK, costed more than £18 billion.[6]

A common feature of underground construction projects is the risk of subsidence as a consequence of the excavation. Whilst current tunnelling technologies enable the ground volume lost during the excavation to be minimised,[7] ground movements cannot be completely avoided, leading to surface differential settlements.[8] These settlements are transmitted through the foundations to the whole building. Depending on the construction material, the building stiffness and the foundation typology, tunnelling-induced settlements can affect adjacent structures with a different level of severity. Evaluating the settlement impact to buildings and structures is a primary concern for the construction industry, and large budgets are usually allocated to (i) monitor building deformations and (ii) estimate the potential building damage.[7,9]

Traditional monitoring techniques utilise established ground-based instruments such as precise levellings, electrolevels, tape extensometers, displacement gauges and robotic total stations.[8,10,11] These instruments enable the inspection of sparse points on the structure, providing a direct measurement of their displacement over time. Due to the high cost of the installation and maintenance of ground-based monitoring systems, only a limited number of buildings are typically monitored.[12] Priority is usually given to buildings with higher historical value and vulnerable structures. As a consequence, the preliminary assessment of settlement-induced damage is typically performed through simplified and over-conservative procedures which neglect some of the most complex yet critical aspects of the problem, like the interaction between the structure and the soil. A conservative preliminary assessment can lead to unnecessary operations, such as more advanced assessments for a high number of buildings—for example , time-consuming finite element analyses - and potential mitigation measures—for example, compensation grouting - with an increase of the final project cost. Furthermore, without the increased availability of monitored building deformations, it is not possible to advance the understanding of the real building response to tunnelling, nor to improve existing damage assessment procedures.

Space-borne interferometric synthetic aperture radar (InSAR) systems operate remotely and, by imaging large areas of the Earth's surface every few days, can provide a high number of measurements with weekly update.[13,14] In particular, recent multi-temporal (MT) InSAR techniques can be used to extract surface deformations over time from long temporal series of InSAR images[15] with millimetre accuracy.[16,17] Such accuracy is comparable with modern robotic total stations, which enable measurements of vertical movements with an accuracy of approximately 1 mm.[18] Several studies looked at the use of MT-InSAR techniques for investigating natural hazards and human-induced processes, such as earthquakes,[19] glaciers,[20] landslides,[21,22] subsidence,[23,24] tectonic motions[25] and volcanic activity.[26–28] Among the available MT-InSAR techniques, Persistent Scatterer (PS) Interferometry[29,30] is capable of extracting temporal series deformations for a high number of points located on buildings and structures.[31] The application of PS Interferometry to buildings,[32–41] archaeological sites,[42] bridges,[43–45] dams,[46–48] railways[49] and roadways[50] and the cross-validation of PS-InSAR-based measurements against GPS,[51–54] traditional levellings[36,38,55–58] and other in situ instruments[46,59–62] demonstrate the reliability of this approach for structural-health monitoring.

Few studies also investigated the possibility to use PS-InSAR for monitoring tunnelling-induced deformations.[36,38,63–67,68] Milillo et al.[38] validated the good quality of PS-InSAR-based measurements for estimating tunnelling-induced settlements. Giardina et al.[36] proposed a PS-InSAR-based approach for the assessment of settlement-induced building damage. The amount of buildings affected by tunnelling excavations, combined with the current availability of PS-InSAR-based measurements, can provide large datasets of field observations previously not available. These datasets can be used for the quasi-real time monitoring of excavation progression and to evaluate trends in structural response to settlements as a function of building characteristics, with the possibility to complement ground-based monitoring systems. Furthermore, PS-InSAR data could be used retrospectively to monitor the buildings which were not equipped with in situ instruments, providing the inputs for more accurate prediction procedures. However, without integration between InSAR techniques and structural models of the building response, the full potential of InSAR monitoring could not be exploited.[37]

In this paper, we present a semi-automated methodology integrating PS-InSAR data and damage assessment procedures to evaluate the settlement-induced building damage in tunnelling scenarios. The methodology combines PS-InSAR-based building displacements and semi-empirical models of the building response to tunnelling to provide a more realistic estimate of the settlement profile for each building. On the basis of the estimated building deformation,

a level of damage is assigned to each building, and damage maps showing the distribution of damage levels for the buildings along the excavation are created. We applied the proposed methodology to a test area of 5 km × 5 km above the Crossrail twin tunnels in central London, UK. Crossrail construction works started in May 2012, and led to the realisation of 10 stations and 21-km tunnel tracks.[69] To minimise the magnitude of ground movements related to the excavation, tunnelling activities were executed by using modern soft-ground pressure-balance tunnel-boring machines. The analysed area refers to an 8.1-km-long segment of the whole Crossrail route, and consists of traditional masonry and framed buildings, built in diverse historical periods and characterised by different types of foundation. We used COSMO-SkyMed PS-InSAR data from April 2011 to December 2015 to reconstruct the displacement field of 858 buildings, obtaining a large dataset of field information on building response to tunnelling. We used this dataset to infer relationships between structural characteristics and building deformations.

The content of the paper is organised as follows. The traditional steps adopted in current damage assessment procedures are reviewed in Section 2.1. A brief overview of MT-InSAR techniques is provided in Section 2.2. Section 3 describes in details the proposed methodology, presenting the required inputs (Section 3.1) and the workflow on which the semi-automated algorithm is based (Section 3.2). A description of the Crossrail case study and the study area is provided in Section 4, while Section 5 presents the results showing a comparison between building levels of damage obtained through the PS-InSAR-based assessment and the greenfield-based assessment. In Section 5.1, the effect of the building position relative to the tunnels on the settlement and vertical displacement is analysed. Finally, in Section 5.2 we used PS-InSAR-based deformation parameters to investigate the building response to settlement for buildings characterised by different structural and foundation systems.

2 | BACKGROUND

2.1 | The traditional damage assessment: A review

Damage assessment procedures are typically used during the design phase to predict the magnitude of the expected settlements and the consequent risk of building damage. Based on this information, mitigation measures can be applied where needed, minimising the tunnelling impact on the existing built environment. Due to the large number of buildings involved, tunnelling-induced damage assessment is traditionally developed as a staged procedure,[70] along which the level of the adopted conservatism is progressively decreased.

The first stage of the assessment enables the identification of structures within the influence area of the settlement.[71]

In the second stage of the assessment, a provisional level of damage is assigned to the buildings identified during Stage 1.[70] Stage 2 uses a semi-empirical method to estimate the ground movements caused by the excavation and calculate the associated building strains. The tunnelling-induced settlement is estimated without accounting for the presence of the structure, an assumption referred to as greenfield condition.[72] According to Peck,[73] the greenfield settlement trough can be modelled as a Gaussian function (Figure 1), and the vertical ground movements $S_v(x)$ are calculated as

$$S_v(x) = \sqrt{\frac{\pi}{2}} \frac{V_L D^2}{4i} e^{-\frac{x^2}{2i^2}}, \tag{1}$$

where D is the tunnel diameter, V_L is the volume loss which corresponds to the percentage of volume loss that occurs at the ground surface during the excavation as a percentage of the total tunnel volume per unit length of tunnel drive, and i is the trough width parameter which corresponds to the horizontal distance between the tunnel centreline and the point of inflection (Figure 1). The trough width parameter i is given by a linear combination of the tunnel depth z and the soil parameter K: $i = Kz$.[74] It is noted that the Gaussian function of Equation (1) is only a first approximation of the effect of ground movements, which is in reality a three-dimensional problem.[75,76] However, three-dimensional effects are usually strong during tunnel progression, while the residual settlement occurring after tunnel completion is well described by bi-dimensional cross sections. The horizontal ground movements can be determined by relating the horizontal displacement $S_h(x)$ to the vertical settlement profile $S_v(x)$, as in O'Reilly and New[74]:

$$S_h(x) = \frac{x}{z} S_v(x). \tag{2}$$

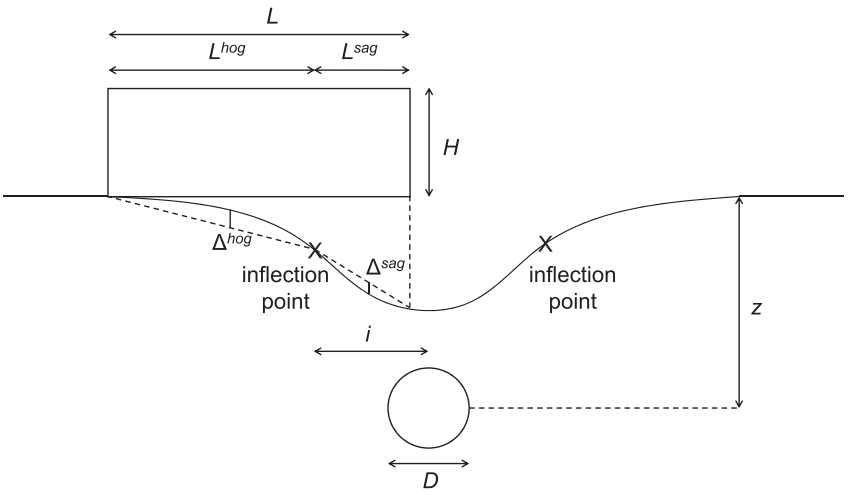

FIGURE 1 Greenfield settlement trough induced by a tunnel of diameter D located at a depth z beneath the ground. The trough width parameter i corresponds to the horizontal distance from the tunnel centreline to the point of inflection on the settlement curve and separates the sagging (sag) from the hogging (hog) zone. The relative deflection, the building length and the building height are indicated with Δ, L and H, respectively

In the second stage assessment, the building is assumed to follow the behaviour of the ground and it is modelled as a weightless, uniform, elastic beam,[77] undergoing sagging and hogging deformations (Figure 1). Relevant building dimensions, L and H, are used in combination with the relative deflection Δ to calculate the maximum bending and diagonal strains, both for the sagging and the hogging zone:

$$\varepsilon_{b,max} = \frac{\frac{\Delta}{L}}{\frac{L}{12t} + \frac{3I}{2iLH}\frac{E}{G}}, \tag{3}$$

$$\varepsilon_{d,max} = \frac{\frac{\Delta}{L}}{1 + \frac{HL^2}{18I}\frac{G}{E}}, \tag{4}$$

The parameter t indicates the distance of the neutral axis from the edge of the beam, under the assumption $t = H$ in the hogging region and $t = H/2$ in the sagging part of the beam. I is the moment of inertia of the equivalent beam, with $I = H^3/3$ in the hogging zone and $I = H^3/12$ in the sagging zone. E and G are the Young's and shear modulus, respectively. The influence of the horizontal ground movements on the building can be measured in terms of the average horizontal strain, which corresponds to the maximum variation in length of the part of the building located in hogging. The average horizontal strain ε_h can be calculated as

$$\varepsilon_h = \frac{\delta^{hog}}{L^{hog}}, \tag{5}$$

where δ^{hog} is the difference between the horizontal displacements at the two ends of the beam located in hogging, and L^{hog} is defined in Figure 1. It should be noted that the part of the beam located in sagging experiences only compressive strains, which are not as dangerous for the structure. Maximum strains, both in bending and shear, are selected by the comparison of the two deformation modes, namely hogging and sagging, and then combined with the horizontal strain, as follows:

$$\varepsilon_{bt} = \varepsilon_h + \varepsilon_{b,max}, \tag{6}$$

$$\varepsilon_{dt} = 0.35\varepsilon_h + \sqrt{(0.65\varepsilon_h)^2 + \varepsilon_{d,max}^2}. \quad (7)$$

The building critical strain ε_c is the highest value between the resultant diagonal strain ε_{dt} and the resultant bending strain ε_{bt}. Depending on the value of the critical strain, the classification proposed by Boscardin and Cording[78] enables the identification of a category of damage. Such classification establishes a link between the estimated building deformation and the possible level of damage, providing an estimate of the settlement impact on the structure. It should be noted that the assumption of a greenfield settlement is typically conservative. Numerical modelling[79–83] and centrifuge testing[84–87] have highlighted how the presence of buildings on the ground tends to flatten the settlement profile. Furthermore, field and experimental observations have indicated that relatively small horizontal strains are typically transferred to the buildings.[8,86,88–90] As a consequence, the greenfield-based approach typically leads to an overestimation of damage.

The third and final stage of the assessment involves time-consuming numerical analysis of the buildings which were predicted to have a moderate or higher level of damage by the second stage assessment.[70] Depending on their structural features, different guidelines and procedures can be adopted. Due to the high conservatism of the working assumption adopted in the second stage of the assessment, buildings that would not need further analysis are sometimes processed in the third stage, leading to a significant increase of the final project cost. The need for a more accurate damage assessment on a city-scale level is a strong motivator for this work.

2.2 | Multi-temporal InSAR

Synthetic Aperture Radar Interferometry (InSAR) is a remote sensing technique which uses the difference in phase between two or more radar images acquired at distinct times to measure surface deformations.[91,92] A typical satellite InSAR system consists of a space-borne radar antenna which is pointed toward the Earth's surface. The looking direction of the satellite radar antenna is called the Line Of Sight (LOS) or slant-range, and its inclination θ relative to the nadir is between 20° and 50°, depending on the satellite platform. Figure 2a shows a simple sketch of a typical InSAR imaging system.

The radar antenna emits an electromagnetic signal in the microwave band toward the Earth's surface. The incident radar signal interacts with the ground, which reflects the signal back to the satellite. The backscattered signal is received and recorded by the onboard radar system and used to generate a SAR image. The area illuminated by the radar on the ground is called the antenna footprint, and it is characterised by a dimension parallel to the satellite orbit, i.e. azimuth, and a dimension orthogonal to the orbit, i.e. slant-range (Figure 2a). A SAR image can be described as a

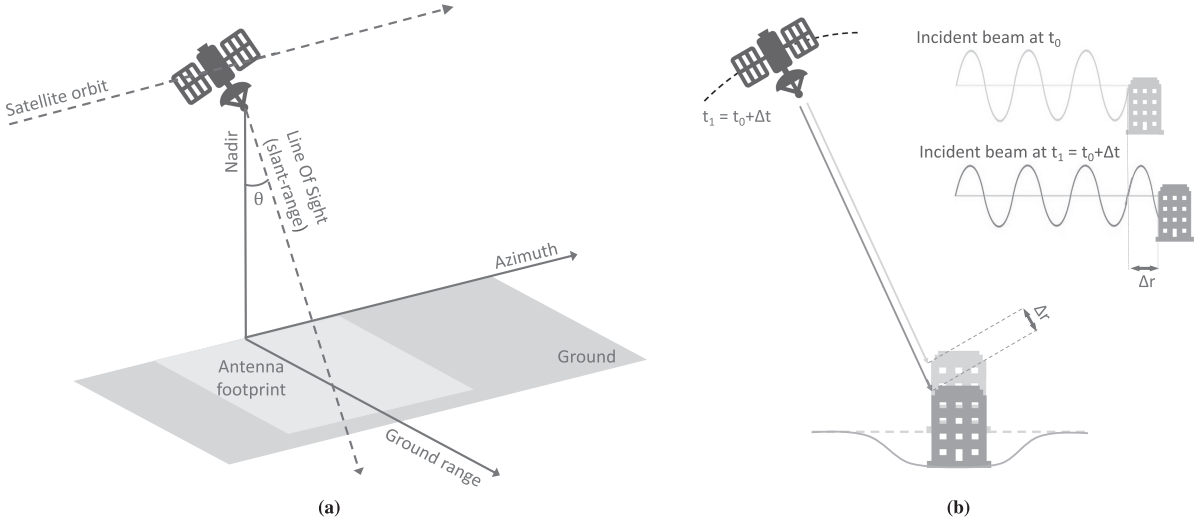

FIGURE 2 (a) Simplified satellite InSAR acquisition geometry. (b) Simplified sketch of the InSAR capability to measure building deformations

bi-dimensional array with the azimuth coordinate in the rows and the slant-range coordinate in the columns. Each element of the array is a pixel which corresponds to a small area of the illuminated surface, and each pixel is characterised by an amplitude and phase information about the backscattered signal. Space-borne InSAR systems are characterised by day-and-night operability, can work in any weather condition and can currently provide images with a spatial resolution up to 1 m and a temporal resolution of a few days.[26]

For simplicity, the radar signal can be approximated to a sinusoidal wave, whereas in reality it corresponds to a chirp characterised by a certain bandwidth. The two-way travel distance between the radar antenna and the target corresponds to an integer number of whole wavelengths plus some fraction of a wavelength. The number of whole wavelengths corresponds to the travel distance taken by the signal to complete a round trip back to the satellite, while the extra fraction of a wavelength depends on the distance of the scatterers to the radar. The phase, Φ, of a given SAR image is the measure of the last fraction of the travel path, and it is proportional to the two-way travel distance of the radiation, $2R$, and the wavelength, λ, of the transmitted signal:

$$\Phi = \frac{4\pi}{\lambda} R. \tag{8}$$

Interferometric SAR (InSAR) techniques can be adopted to retrieve relative displacements from two SAR images of the same area, acquired in different times.[14] If a point on the Earth's surface moved between the two acquisitions, such movement produces an extra fraction, Δr, of the wave radar signal (Figure 2b) which is then reflected and recorded. This extra fraction of wavelength produces a phase difference between the two acquisitions, which can be used by InSAR techniques for the retrieval of the occurred displacement. The phase difference $\Delta\Phi$ is proportional to Δr divided by the wavelength λ of the signal:

$$\Delta\Phi = \frac{4\pi}{\lambda} \Delta r. \tag{9}$$

Whilst traditional InSAR is based on a two-image configuration, recent MT-InSAR techniques enable the analysis of long series of InSAR images.[15,30] In particular, Persistent Scatterer Interferometry (PSI or PS-InSAR)[29,30] is a powerful signal processing technique which enables the retrieval of the temporal and spatial evolution of surface displacements, located on ground and structures, from long temporal series of InSAR images.[93] PS-InSAR is based on the identification of natural reflectors which remain stable within the time series of InSAR images. These natural reflectors, called permanent or persistent scatterers (PSs), are commonly identified in architectural elements and metallic structures, making PS-InSAR extremely effective in urban areas.[31]

However, PS-InSAR typically provides a huge amount of measurements for different targets, such as buildings, bridges and roadways, located within the monitored area. To evaluate the structural condition of specific buildings, such measurements need to be analysed in combination with large building databases and structural models. When a large number of buildings is involved, like in underground construction projects, only an automated integration of PS-InSAR-derived displacements, building geo-spatial databases and building structural models can provide useful building information at city-scale level.

3 | METHODOLOGY

We developed a semi-automated methodology based on the integration of PS-InSAR-based displacements and damage assessment procedures to predict the risk of damage to buildings adjacent to tunnel excavations. The developed methodology combines satellite radar interferometric data, geotechnical information and a Geographical Information System (GIS)-database of building features. Specifically, PS-InSAR-measured displacements were used to estimate the actual settlement profile for each building. This curve was used to quantify the soil–structure interaction, which is typically neglected during current assessment procedures. On the basis of the maximum building strain, we assigned a level of damage to each building, and produced damage maps showing the distribution of building damage along the excavation. Results were compared with the damage based on the traditional greenfield procedure. Details about the datasets used as an input and the processing chain are presented in Sections 3.1 and 3.2, respectively. Their dependencies are shown in the flowchart of Figure 3.

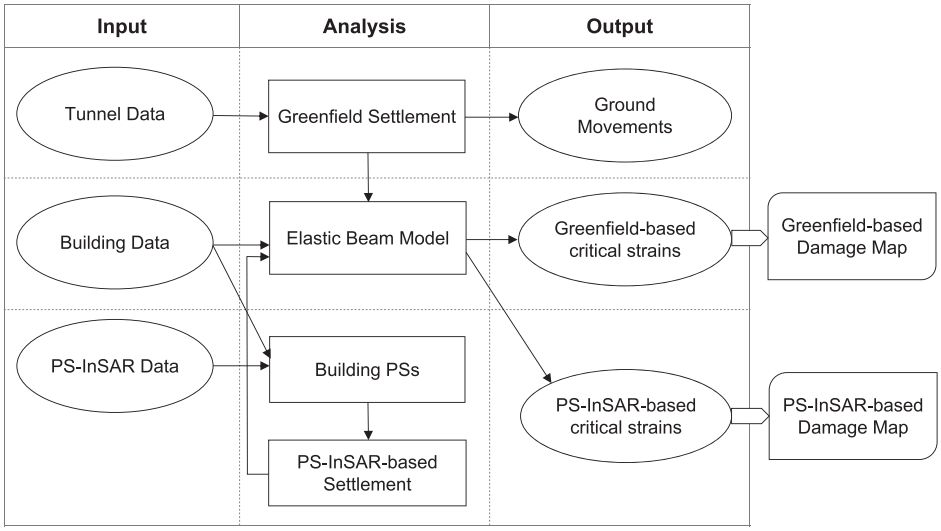

FIGURE 3 Flowchart describing the developed methodology

3.1 | The input datasets

The proposed methodology requires three datasets as an input:

1. tunnel and soil features, i.e. diameter D, local depth z, measured values of volume loss V_L and trough width parameter K;
2. building geometrical dimensions and characteristics, i.e. structural typology, foundation type and historical age;
3. PS-InSAR-based displacements.

3.1.1 | The tunnel dataset

We applied the proposed methodology to the Crossrail tunnel excavation in London, UK, analysing an 8.1-km-long segment of the alignment between the stations of Paddington and Liverpool Street (Section 4). The Crossrail alignment is characterised by two tunnels of 7.18-m diameter and a variable depth, up to 40 m. Since the tunnel depth z can vary considerably along the route, geometrical data related to different tunnel sections were interpolated to reconstruct the whole tunnel geometry, establishing a precise correspondence between the monitored buildings and the local depth of the tunnel. The soil parameter K, which is used to calculate the tunnel trough width i (i.e., $i = Kz$), depends on the type of soil in which the tunnel is excavated.[71,74] Thanks to levelling measurements at the ground level along the transects, measured values of the soil parameter and the volume loss were available for several tunnel sections in Drive X, while between the stations of Farringdon and Liverpool Street (beginning of Drive Y) we had no measurements. Consequently, for the buildings located in Drive X we interpolated the available measurements along the different tunnel sections and used punctual values of K and V_L, while for the buildings located in Drive Y (13% of the total) these two parameters were approximated to the average of measured values. For the soil parameter we obtained an average of 0.5 and a standard deviation of 0.1. For the volume loss we found an average of 0.7% and a standard deviation of 0.3%.[12,36]

3.1.2 | The building database

The building database contains the footprints of the buildings along the tunnel track, and provides for each building geographical coordinates and additional information, including the construction material, the period in which the edifice was built and the type of foundation.

A GIS layer containing the geographical extent of the PS-InSAR data were used to extract from the building database only the buildings within the monitored area. The information contained in the building database was used to create three different GIS layers. In each layer, we grouped the buildings on the basis of structural typology, type of

foundation and age of construction, according to the classes of interest defined in Table 1. The classification used for the age of construction was based on the criteria adopted in the UK for recognising historical value buildings.[94]

The building footprints were processed to obtain the geometry of each building, which was used as an input in the developed algorithm. Since adjacent buildings with the same construction properties and similar geometrical features respond to the settlement as a unique structural block, we were interested in the identification of independent structural units. The layers previously defined, i.e the structural typology layer, the foundation type layer and the period of construction layer, were overlaid in the GIS environment to identify buildings sharing similar features and recognise buildings which are part of the same structural block. The footprints of the interconnected buildings were merged to create a single geometry. Furthermore, since the algorithm implements the equivalent beam model proposed by Burland and Wroth,[77] the building footprints were simplified and each geometry was approximated to the closest quadrilateral. Buildings with central holes were treated as full buildings and complex shapes, such as "L" shapes, were cut. These simplifications are in line with the assumptions typically adopted in the second stage assessment (Section 2.1) and are expected to have a negligible effect on the final results. An example of a building footprint before and after the processing is shown in Figure 4.

TABLE 1 Classes of interest for the analysed buildings

Parameter	Classification
Age	Pre-1700
	1700–1840
	1840–1945
	Post-1945
Structure	Load-bearing masonry
	Framed
Foundation	Shallow
	Piled

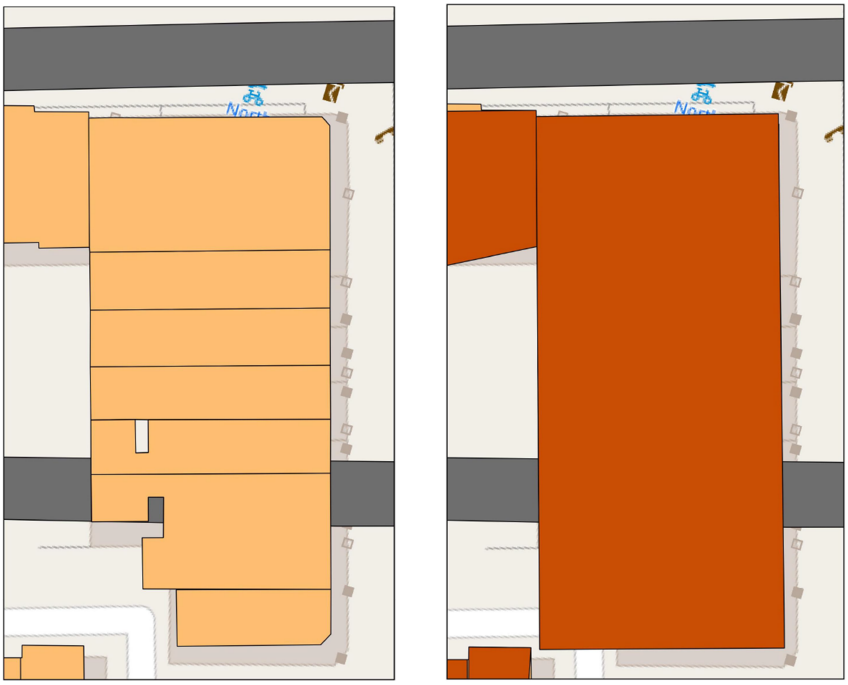

(a) (b)

FIGURE 4 Building footprint (a) before and (b) after the processing

Similarly, structural details of roof, foundations and facade opening, such as windows and door, were neglected. These simplifications can lead to conservative results. A higher level of detail is adopted in the third stage of the assessment (Section 2.1), where each building is analysed separately through complex finite element models.

3.1.3 | The PS-InSAR dataset

The PS-InSAR dataset was obtained by processing 72 descending images acquired between April 2011 and December 2015[38] by the COSMO-SkyMed constellation. The COSMO-SkyMed constellation includes four identical satellites with a 16-day revisit time each. COSMO-SkyMed satellites are equipped with X-band SAR antennas (3.1-cm wavelength), enabling the measurement of surface deformation with 3-m resolution.[26] The series of InSAR images was processed by implementing the PS-InSAR time series analysis (Section 2.2) through the use of the SARPROZ software package,[95] which enabled the identification of PS points within the analysed area.

The interferometric data refer to an area of about 5 km × 5 km in central London. The dataset contains the coordinates of points extracted from the series of InSAR images, as well as the estimated elevations, average deformation velocities, cumulative displacements and displacement time series. The accuracy of the PS-InSAR data used in this work was validated through comparison with measurements acquired by Precise Levelling Points.[36,38] Figure 5 shows the map of cumulative displacements along the satellite LOS obtained after the time series analysis. Negative values correspond to PSs moving away from the satellite and positive values refer to displacements toward the satellite. Red and orange points indicate large movements associated with ground settlement above the Crossrail twin tunnels.

3.2 | The processing algorithm

The automated algorithm presented in this paper was built on the methodology proposed by Giardina et al.[36] The three datasets described in Section 3.1, i.e. the tunnel geometry, the database of building features and the PS-InSAR dataset, were used as an input of the developed methodology. The workflow of the developed methodology is based on the

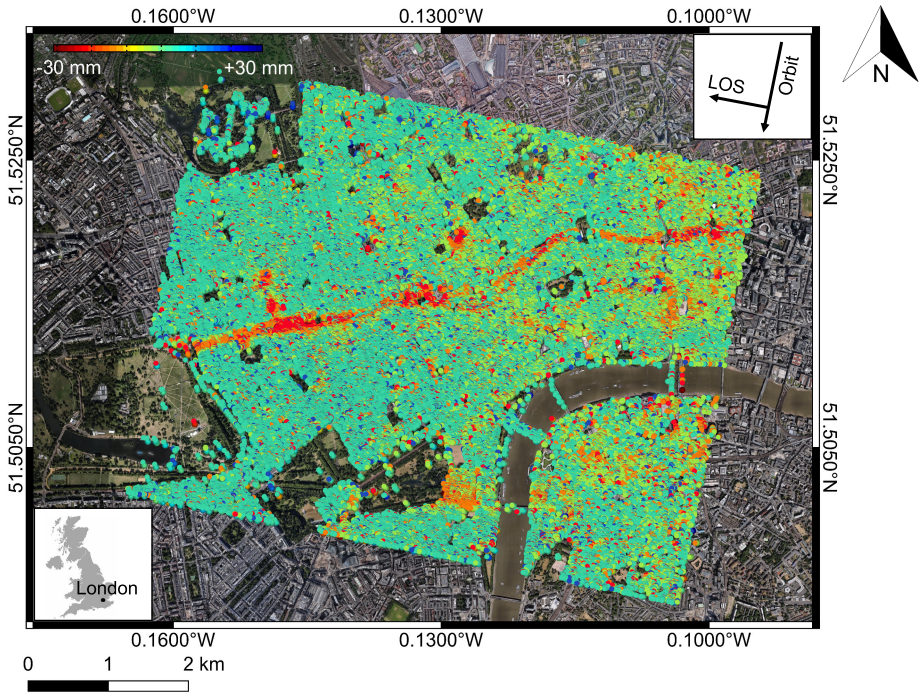

FIGURE 5 Cumulative displacement map of the analysed area in London, obtained by processing COSMO-SkyMed data between 2011 and 2015.[38] The map shows the distribution of the cumulative displacements measured along the satellite LOS over the Crossrail route. Each point corresponds to a permanent scatterer

procedure adopted in the second stage assessment (Section 2.1), with the innovation that PS-based building displacements are used to perform a more realistic prediction of the building level of damage.

In the first step, we assumed that each tunnel generates a Gaussian shaped settlement.[73] The soil parameter K, the volume loss V_L, the tunnel diameter D and the tunnel depth z, defined as in Section 3.1.1, were used to calculate the greenfield settlement profile for each tunnel (Equation 1). These settlement profiles were calculated disregarding the influence of surface structures, i.e., under the greenfield assumption. Depending on the distance between the tunnel centrelines, the effect of the twin tunnels was combined as defined in the Crossrail second phase assessment.[96] Figure 6 shows the three possible configurations. If the separation between the tunnel centrelines is less than $2i$, two hogging zones and one sagging zone are identified, i.e. the three-zone scenario of Figure 6a. If the separation is between $2i$ and $6i$, three hogging zones and two sagging zones are recognised, i.e. the five-zone scenario of Figure 6b. If the tunnel centrelines are $6i$ apart, four hogging zones and two sagging zones can be observed, i.e. the six-zone scenario of Figure 6c. In this latter case, the two tunnels act like independent tunnels.

In the second step, the building footprints, which were defined in Section 3.1.2, were used to identify all the PSs within the corresponding building aggregate. To identify only scatterers belonging to the building and not to the ground, only PSs with an elevation of more than 5 m with respect to the ground level were selected. Furthermore, to guarantee the reliability of processed measurements, only PSs with a coherence greater than 0.8 were selected. Building PSs were processed to remove any phase unwrapping error and ground reference point offset, as in Giardina et al.[36] It should be noted that the PS-InSAR-based displacements correspond to movements of the monitored radar targets measured along the satellite LOS in the elapsed time. Since for the specific case of tunnelling-induced settlements vertical displacements are dominant, we processed the InSAR-based LOS displacements within the assumption of zero horizontal movements.[97] As a consequence, vertical displacements were obtained by projecting the LOS displacements into the vertical direction with the use of the radar incidence-angle, which is 30° in our specific case.

In the third step, we used the PS-InSAR-based displacements to quantify the actual building deformation. Building PSs belonging to the same block of connected edifices were interpolated over the building length using a modified Gaussian function.[36] The modified Gaussian function is based on the greenfield settlement profile which was calculated in the first step of the method. Only buildings with at least three available PSs were included in the analysis. The fit-based profile allowed the determination of three fitting coefficients α, β and γ, which were used to generate three modified parameters: the modified horizontal coordinate, $x_m = \alpha + x$, the modified volume loss, $V_{L,m} = \beta V_L^{eb,wb}$ and the modified trough width, $i_m = \gamma i$. Such parameters enabled the retrieval of a more realistic settlement profile for each building. The modified parameters were introduced in Equation (1) to obtain the modified settlement equation:

$$S_m(x) = \sqrt{\frac{\pi}{2}} \frac{D^2}{4 i_m} V_{L,m} e^{-\frac{x_m^2}{2 i_m^2}} \tag{10}$$

The PS-InSAR-based settlement was used to estimate deflection ratios for each building aggregate.

The fourth step aims to retrieve the building strains from the PS-InSAR-based deflection ratios. Each building aggregate was modelled as a weightless, linear elastic beam of length L, height H and unit thickness.[77] The building height H was estimated by using the elevation of the PSs located on the building roof. A material parameter $E/G = 2.6$ was assumed for all the buildings, as in Crossrail.[96] The parts of the structure undergoing hogging and sagging deformations

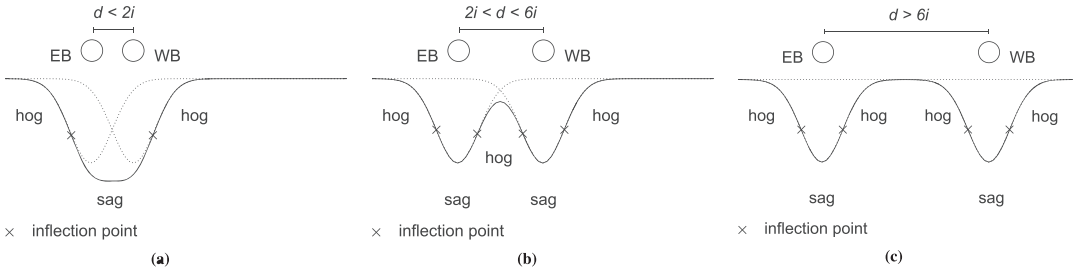

FIGURE 6 Three possible scenarios for the settlement trough given by the combination of two tunnels (after Crossrail[96] and Giardina et al.[36]): (a) three-zone scenario, (b) five-zone scenario and (c) six-zone scenario. d corresponds to the horizontal distance between the centrelines of the Eastbound (EB) and Westbound (WB) tunnels

were analysed separately. Timoshenko's equations[98] were used to calculate the bending strain, ε_b, and the shear strain, ε_d, for each sagging and hogging part (Equation 3–4). Then, we calculated the building critical strain as defined in Section 2.1. The building critical strain was used to estimate the building level of damage, according to an adapted version of the classification proposed by Boscardin and Cording,[78] as defined in Section 5.

In the fifth and final step of the algorithm, the building levels of damage were stored in the attribute table of the building-GIS layer used as an input (Section 3.1.2), and damage maps were generated.

It should be noted that the fit-based approach defined in step 3 enables the evaluation of the influence of the building on the settlement trough, providing a quantification of the soil–structure interaction. To compare the performance of the PS-InSAR-based prediction with the traditional greenfield-based approach, the Steps 1, 3, 4 and 5 were used to perform a greenfield-based assessment, and building deflection ratios were estimated from the greenfield settlement profile.

4 | THE CROSSRAIL CASE STUDY

The methodology presented in Section 3 was used to assess the structural damage to buildings located above the Crossrail twin tunnels in London, UK. The entire Crossrail alignment runs from Royal Oak to Pudding Mill Lane and Plumstead (Figure 7a) and consists of 21-km twin tunnels of 7.2-m diameter and up to 40-m depth. This work relates to a 5 km × 5 km sub-area of the total Crossrail route. The area is between Paddington and Liverpool Street, and covers most of the Drive X section and the beginning of Drive Y, as shown in Figure 7a.

In the monitored area, the local soil shows a stratigraphy given by layers of Terrace Deposits, London clay, the Lambeth Group, Thanet sands and Chalk, as schematised in Figure 7b. The geological section of Figure 7b shows that the London Clay is at its thickest in Paddington Station. Then, the interface between the London Clay and the underlying Lambeth Group rises and the tunnels become deeper, reaching their maximum depth in Liverpool Street. The Lambeth Group and the Thanet sands typically present some difficulties for tunnelling. The hydrogeology of the London area is mainly controlled by two aquifers, commonly referred to as the upper and lower aquifers. The piezometric surfaces are at approximately zero Ordnance Datum (OD), that is, 5–6 m below the ground level, and between −40 and −50 m OD, respectively.[9] Due to the different ground features and groundwater conditions, diverse tunnelling methods were adopted. Specifically, the excavation was executed by using slurry tunnel-boring machines in the London Clay and by using earth pressure-balance tunnel-boring machines in the Lambeth Group. To limit possible ground subsidence, compensation grouting was adopted in several locations during the excavation.

The monitored area in London is exceptionally rich in buildings with a wide range of features, such as masonry buildings of historical value and from different periods and styles, and modern framed buildings, relying on piles or shallow foundations. Most of the historical buildings belong to the Victorian age or to the early 20th century, but there are also several Georgian houses and a few older buildings.[99] Specifically, the area between Paddington Station and Bond Street is home of many Grade II listed buildings, as well as from Fisher Street Shaft to Farringdon Station. A few Grade I buildings are around Bond Street and Tottenham Court Road Station, while some other structures in the zone have been designated

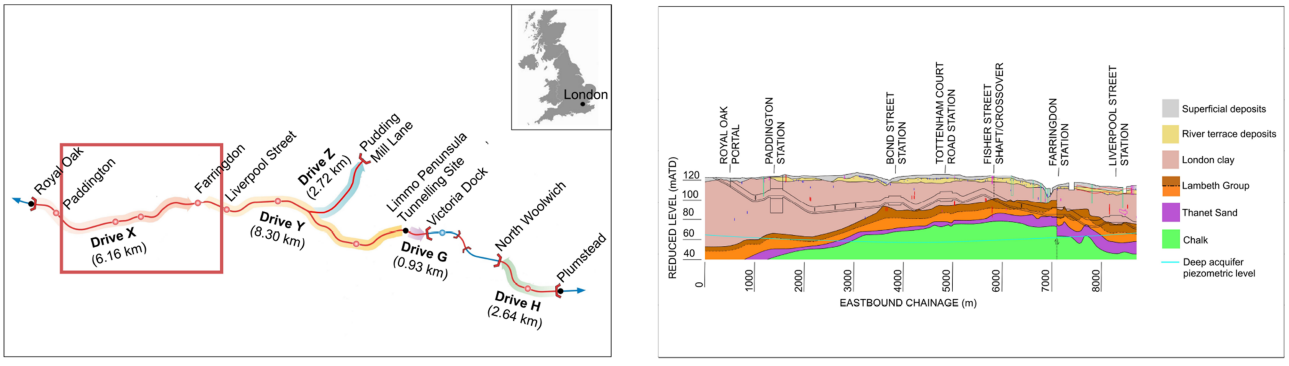

FIGURE 7 (a) Location map and overview of the Crossrail alignment in London; the rectangle highlights the study area, which is between Paddington and Liverpool Street. (b) Longitudinal geological cross-section of the Crossrail route from Royal Oak to Liverpool Street[96]

as Grade II* listed buildings. Georgian buildings generally show regular and symmetric shapes and are mainly organised in rows of terraced houses. Victorian buildings can be found as detached houses or in terraces. For both Georgian houses and Victorian buildings, the construction materials are typically bricks and local stones.

Survey activities, assessments, monitoring, intervention works and soil investigations cost Crossrail about £1 billion. To identify the type of structures potentially affected by the settlement,[96,100] a high number of studies and monitoring activities were carried out before the tunnelling construction. Looking at the potential interaction between adjacent structures in blocks of buildings, Crossrail identified the following configurations of interest:

- isolated masonry buildings with lime mortar, uniform facades and small openings were expected not to be very sensitive to the settlement;
- masonry structures with large openings and located between stiffer framed buildings were expected to be susceptible to small movements;
- buildings which concentrate all their movements in one location as a consequence of their structural form, were expected to have a higher probability of cracking.

Thousands of buildings were initially assessed using a procedure based on the Limiting Tensile Strain Method (LTSM) developed by Burland and Wroth,[77] meaning that the stiffness of the structures was neglected until the last stage of the assessment.[96] To deal with buildings affected by the settlement, a detailed plan for post-construction surveys and commitments to repair damage which tunnelling operations have caused was developed.[100]

5 | RESULTS AND DISCUSSION

To investigate the effects of the excavation on different building categories, the buildings within the monitored area were reported in a Geographic Information System (GIS) and classified on the basis of structural typology, foundation type and age of construction, as defined in Section 3.1.2. Figure 8 shows the results of the classification based on age of construction. Results indicate that more than 50% of the analysed buildings were constructed between 1840 and 1945. Georgian houses and more ancient buildings represent about 6% and 2% of buildings, respectively. About 8% of buildings were built after 1945, and mainly consist of large concrete framed structures, relying on piles or deep foundations. For the remaining 35% of buildings, the period of construction is not known.

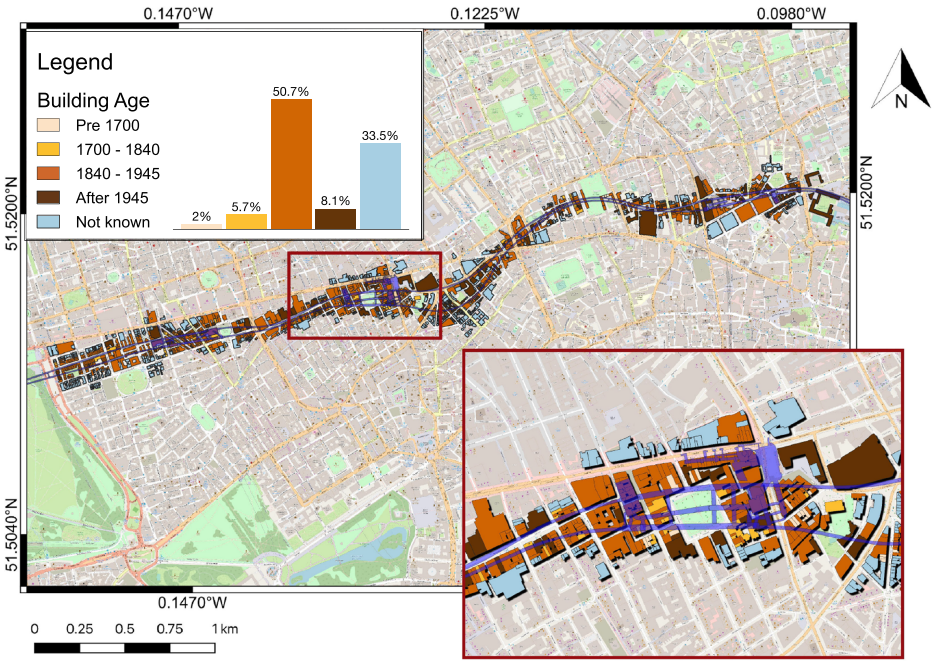

FIGURE 8 Age-based classification of the buildings between Paddington and Liverpool Street, along the Crossrail twin tunnels in central London. The Crossrail alignment is represented with a blue line

Figure 9 shows the distribution of the structural typologies and foundation types for the buildings within the monitored area. The classification is based on the classes of interest defined in Section 3.1.2. About 44% are masonry structures, 17.6% are framed structures, and for about 39% of buildings the structural type is unknown. Furthermore, 58.7% of buildings were built on shallow foundations, 5.3% of buildings are resting on piles, and for the remaining 36% of buildings the foundation type is unknown.

The integration of the PS-InSAR dataset with the building database led to the identification of 9146 PSs on the analysed buildings, corresponding to an average of six PSs per structure. The distribution of the number of PSs identified for each structure is shown in Figure 10. Specifically, three or more PSs were identified for about 55.6% of structures, one or two PSs for 18.6% of buildings and 25.8% of buildings did not show a PS. Since ground-based sensors were only installed on a few tens of structures along the tunnel, the possibility to identify at least one PS for about 74% of buildings is the first notable achievement of the proposed methodology. Furthermore, it is noted that only one acquisition geometry was used in this analysis. The combined use of ascending and descending acquisition geometries can provide an even higher number of PSs per building.

The GIS layers in Figures 8 and 9 were used to identify the buildings which are part of the same structural block (Section 3.1.2), leading to the identification of 1153 independent building aggregates. These buildings were processed using the algorithm described in Section 3.2. To perform a reliable fit, only building aggregates with at least three PSs were selected, accounting for a total of 858 buildings. The PS-InSAR-based assessment demonstrated that the buildings within the monitored area experienced a 'negligible' risk of damage.[101] To relate the building critical strains to the level of severity, an adapted version of the classification proposed by Burland et al.[101] was adopted. Three ranges of maximum deformations were identified and used to define three categories of damage, that is, A, B and C, which increase in level of severity. Then, critical strains calculated for each building aggregate were associated with the corresponding level of damage, as described in Section 3.2. The results were used to generate the damage maps shown in Figure 11. Specifically, Figure 11a shows the damage classification obtained through a greenfield-based assessment, while Figure 11b refers to the damage prediction based on the PS-InSAR-based assessment. The maps highlight that the greenfield-based assessment overestimates the predicted damage level. In the greenfield scenario, 43% of buildings experienced the highest category of damage, that is category C, 12% of buildings fit category B, and 45% of buildings fit category A. The PS-InSAR-based assessment led to 38% of buildings experiencing critical strains in the range associated with category C, 16% of buildings falling into category B, and 46% of buildings fitting the lowest category damage, that is A. Building critical strains used to retrieve the damage levels shown in Figures 11a,b, were calculated by considering

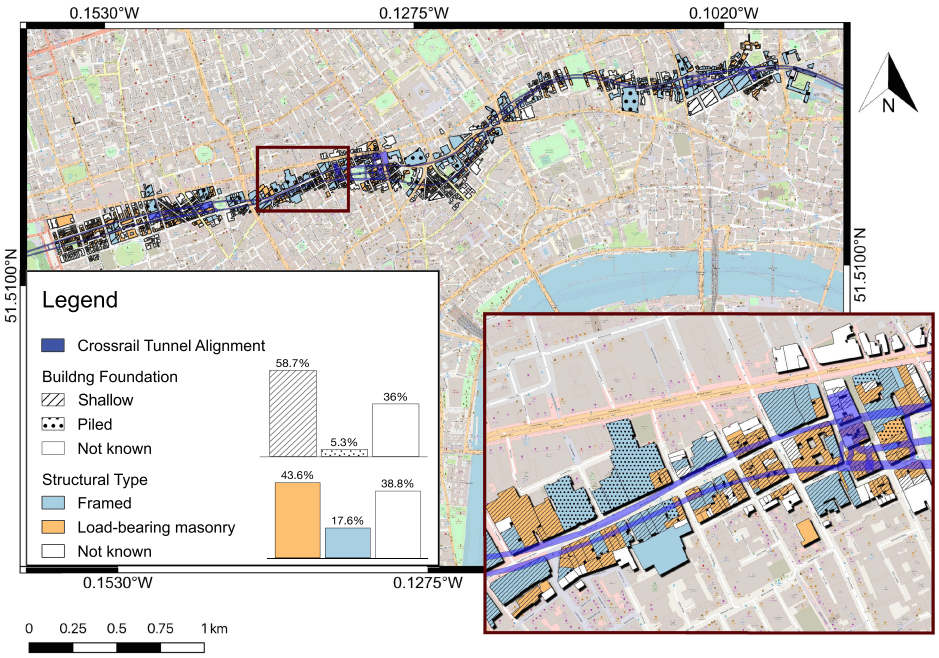

FIGURE 9 Classification based on the structural typology and the foundation type of the buildings between Paddington and Liverpool Street, along the Crossrail twin tunnels in London. The Crossrail alignment is represented with a blue line

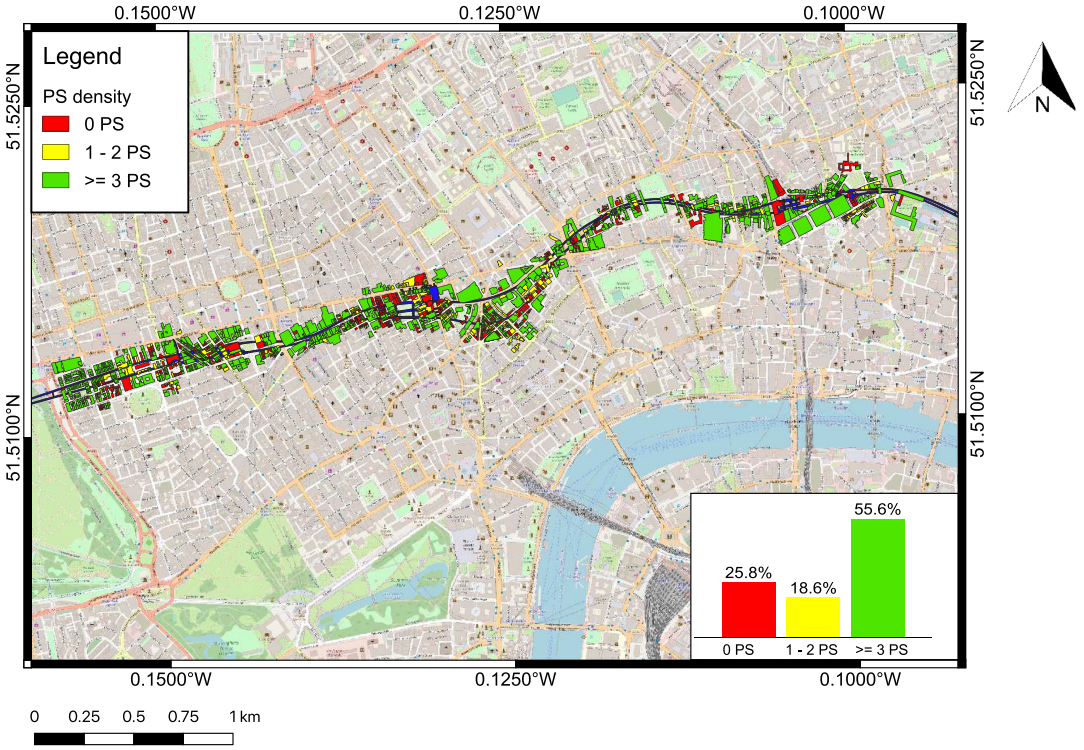

FIGURE 10 PS density on the buildings between Paddington and Liverpool Street, along the Crossrail twin tunnels in London. The Crossrail alignment is represented with a blue line

only the contribution of the vertical settlement, based on the assumption that most of the deformations occur vertically, and that relatively small horizontal strains are typically transferred to the building, as reported in Section 2.1. Furthermore, the strain calculation was based on the use of a unique material parameter E/G for all the buildings (Section 2.1). It should be noted that given the higher flexibility of framed structures, several authors suggested different E/G values, e.g. 12.5,[102] for this class of buildings. As the scope of this study is to show a comparison between the InSAR-based results and the greenfield-based assessment, and no definitive consensus exists on the E/G value to be used for framed structures,[103] $E/G = 2.6$ was adopted for all the buildings. However, the developed procedure is flexible to the use of different E/G values for different structures. As an example, when a value of $E/G = 12.5$ is used for framed structures, for these buildings we observed a reduction of the critical strains up to 50%.

5.1 | Effects of the building-tunnel position on vertical cumulative displacement

Thanks to the high density of InSAR measurements and their automated integration with building data, it was possible to analyse settlement profiles for buildings with different structure, foundations, and position relative to the tunnels, and identify trends in the building behaviours.

As an example, Figure 12 shows four buildings with different structural typology and position relative to the tunnels: one is a framed building with unknown foundation type and symmetric position relative to the tunnels, one is a load-bearing masonry building on pile foundations and with symmetric position relative to the tunnels, and two are framed buildings, both on pile foundations and entirely positioned on one side of the tunnels.

Figure 13 shows four framed structures positioned asymmetrically to one of the tunnels and with one end located above or nearly above one of the settlement trough minima: three of them are on shallow foundations, and one is on piled foundations.

It is noted that for most of the cases in Figures 12 and 13, the presence of the building led to a flattening of the settlement curve. However, this does not necessarily imply a reduction of the magnitude of vertical settlements.[104] As an example, the buildings in Figure 13 experienced a vertical displacement larger than the equivalent greenfield. These observations match results obtained through centrifuge tests for the same building-tunnel configurations.[86]

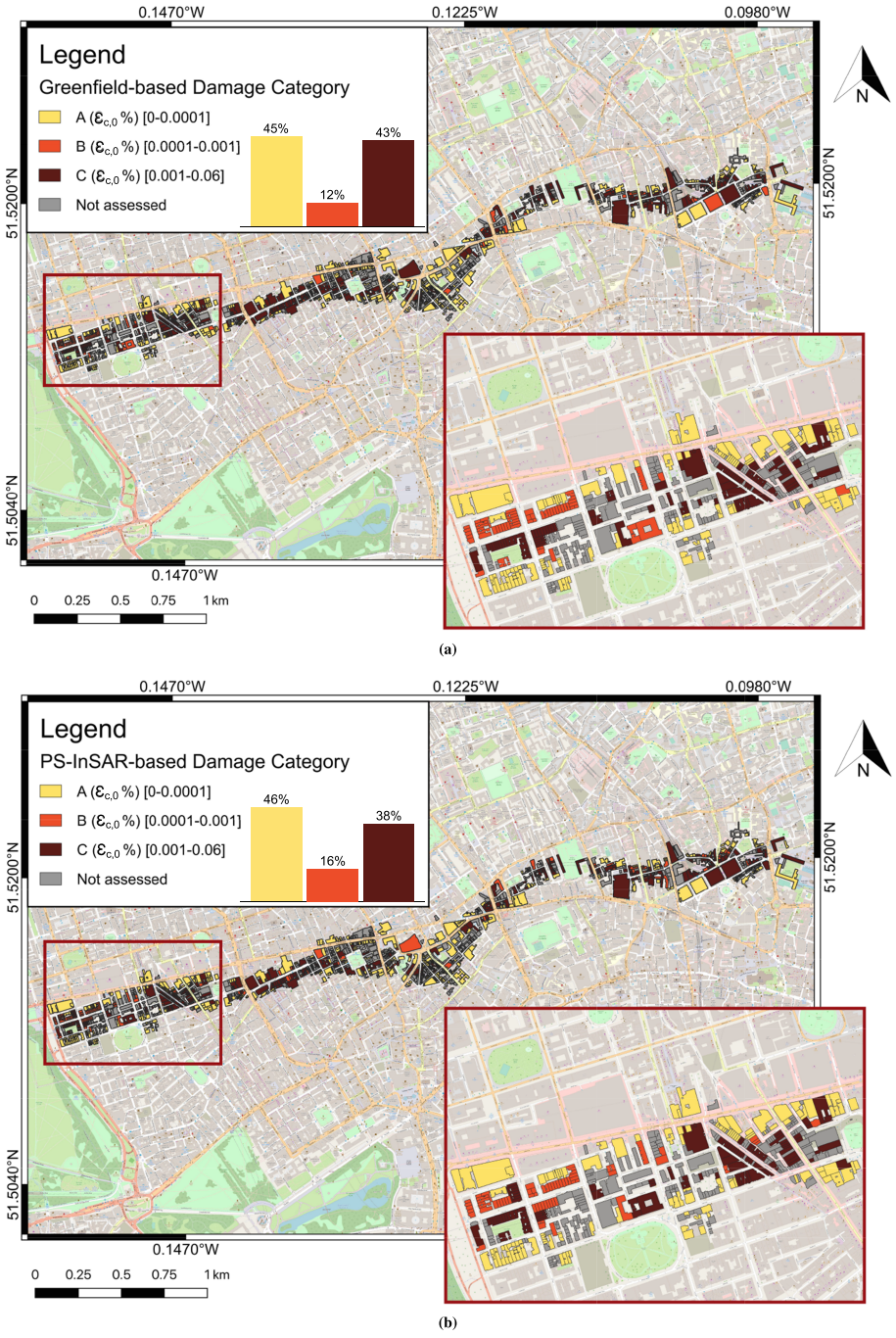

FIGURE 11 Damage maps for the buildings between Paddington and Liverpool Street, along the Crossrail twin tunnels in London. The building levels of damage are based on the building critical strains calculated through (a) the greenfield-based assessment and (b) the PS-InSAR-based assessment. $\varepsilon_{c,0}$ indicates the building critical strain calculated by neglecting the horizontal component

5.2 | Effects of building stiffness on deflection ratio

The availability of PS-InSAR-based measurements for a large number of buildings enabled the investigation of the building response to tunnelling-induced settlement in relation with building deformation parameters, for buildings characterised by different structure, i.e., masonry or framed, and foundations, i.e., shallow foundations or piles.

Figure 14a,b show the building deflection ratios against the height-to-length ratio H/L for hogging and sagging deformation, respectively. Both load-bearing masonry and framed buildings on shallow foundations exhibit larger deflection ratios for H/L values smaller than one, as the building geometry makes them more vulnerable to

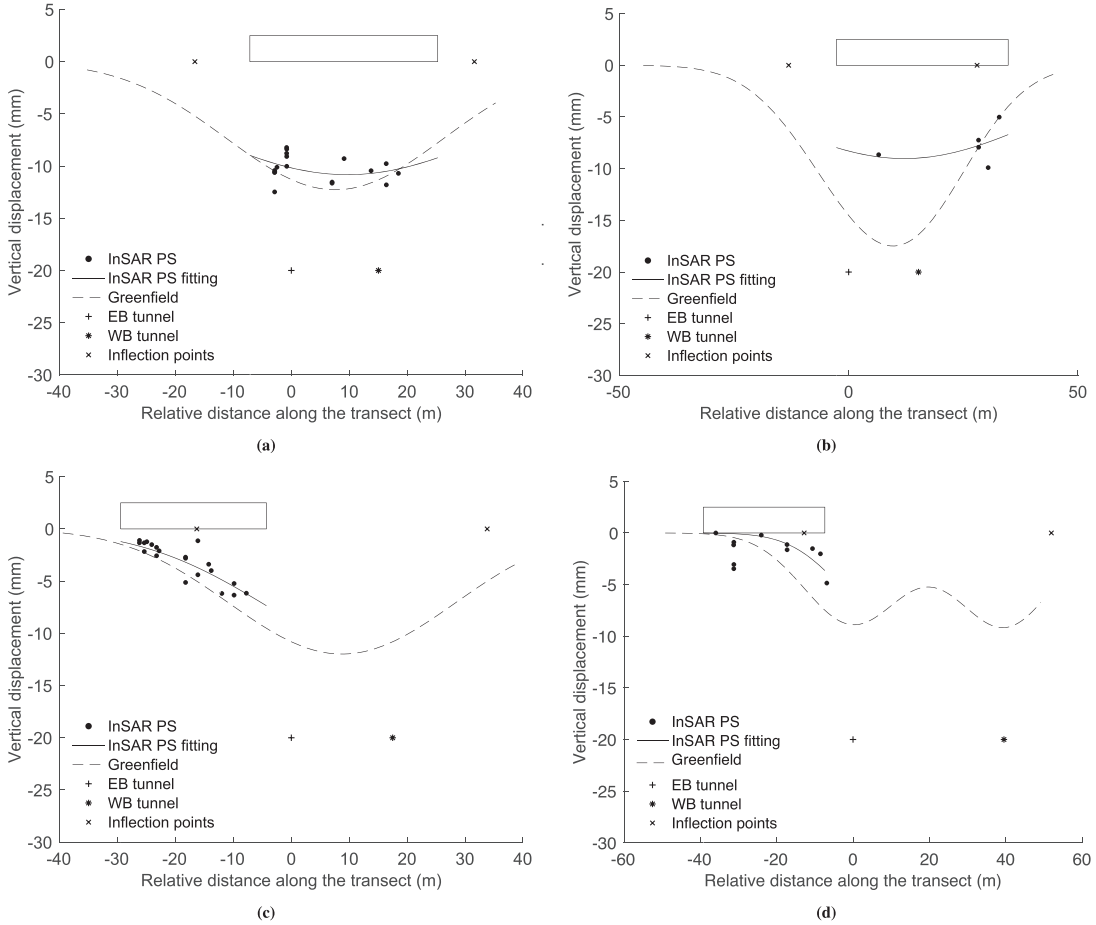

FIGURE 12 Examples of building effects on vertical settlements: (a) framed building with unknown foundation type and symmetric position relative to the tunnel, (b) load-bearing masonry building on pile foundations and symmetric position relative to the tunnel, (c) framed building on pile foundations and positioned on the side of the tunnels, and (d) framed building on pile foundations and positioned on the side of the tunnels. V_L and K were measured at (a) 157 m, (b) 22 m, (c) 120 m and (d) 78 m from the respective building. The building rectangles correspond to the projection of the medium building sections along the transect. Though some PSs can exceed the projected building section, they are part of the building footprint and can be found in buildings characterised by a non-zero alignment with respect to the tunnel axis

deformations. Furthermore, greenfield-based deflection ratios are typically higher than actual deflection ratios, especially in sagging and for lower values of H/L (Figure 14b).

To compare the building response to settlement for load-bearing masonry and framed buildings on shallow foundations, we implemented a fit on the values of the deflection ratio shown in Figure 14a,b. We defined our fit function on the basis of the Timoshenko's equation for an idealised central point loaded (P) beam:

$$\frac{\Delta}{L}=\frac{PL^2}{48EI}\left(1+\frac{18EI}{L^2HG}\right) \tag{11}$$

where, $I_{hog}=H^3/3$ and $I_{sag}=H^3/12$ are the moments of inertia for hogging and sagging, respectively, and P is the applied load. If we distinguish between hogging and sagging, and assume that $x=H/L$ is the independent variable, $a=p/E$ and $b=E/G$ are the fit coefficients, where p is the load applied per meter of beam, i.e., relative load, Equation (11) leads to the following fit functions:

$$\left(\frac{\Delta}{L}\right)^{hog}=\frac{a}{16}\frac{1}{x^3}\left(1+6bx^2\right), \tag{12}$$

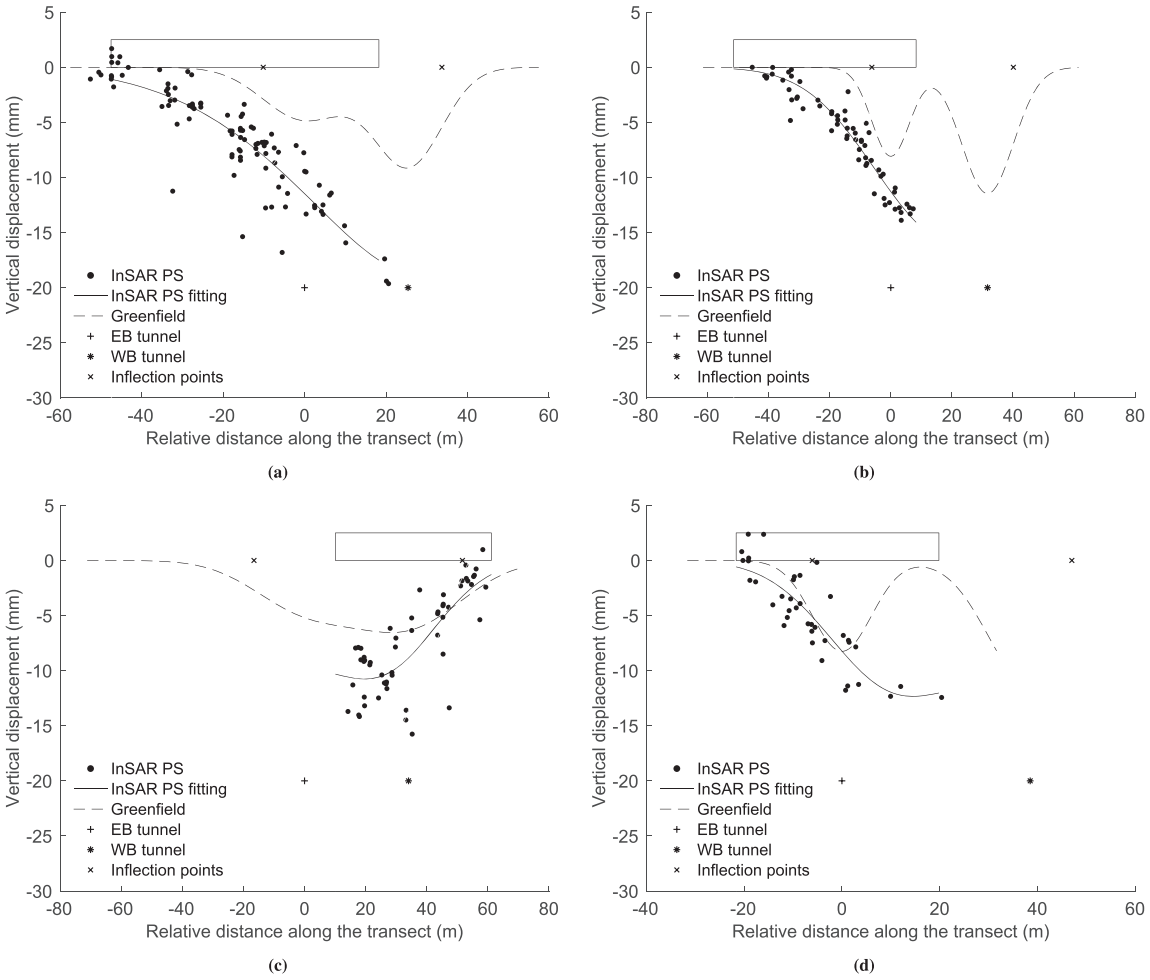

FIGURE 13 Examples of building effects on vertical settlements for buildings positioned asymmetrically to one of the tunnels and with one end located above or nearly above one of the settlement trough minima: (a) framed building on shallow foundations, (b) framed building on pile foundations, (c) framed building on shallow foundations and (d) framed building on shallow foundations. V_L and K were measured at (a) 16 m, (b) 9 m, (c) 1 m and (d) 65 m from the respective building. The building rectangles correspond to the projection of the medium building sections along the transect. Though some PSs can exceed the projected building section, they are part of the building footprint and can be found in buildings characterised by a non-zero alignment with respect to the tunnel axis

$$\left(\frac{\Delta}{L}\right)^{sag} = \frac{a}{4}\frac{1}{x^3}\left(1+\frac{3}{2}bx^2\right). \tag{13}$$

We constrained the fit coefficients a and b to ranges larger than realistic intervals: $1*10^{-7} < a < 1*10^{-3}$ and $2 < b < 100$, which were selected on the basis of numerical tests and literature values. The coefficients returned by the fit are shown in Table 2, and quantify the different response of analysed building categories in terms of global flexibility.

The corresponding fit curves in hogging and sagging are shown in Figure 15a,b, respectively. For each deformation mode, load-bearing masonry buildings show lower values of p/E, indicating that for similar values of p they are stiffer than framed structures. Similarly, load-bearing masonry buildings show E/G values lower than framed buildings. The difference is larger in hogging than in sagging. The curves of Figure 15 reflect the different stiffness between the two classes of structures, highlighting the different behaviour in hogging and sagging.

We then compared actual and greenfield deflection ratios for buildings with the same structural and foundation typology. Figures 16 and 17 show the actual and the greenfield deflection ratio, in hogging and sagging, for load-bearing masonry and framed buildings, respectively, on shallow foundations. Figures 18 and 19 show the same parameters for

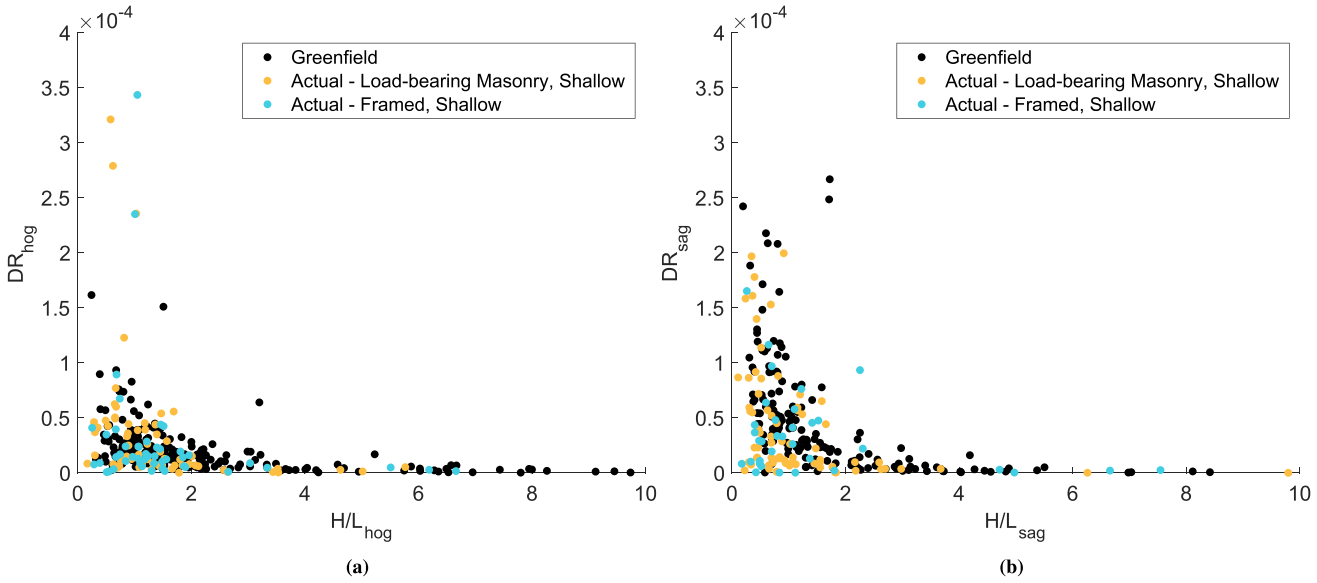

FIGURE 14 Deflection ratio DR against the building aspect ratio H/L (a) in hogging and (b) in sagging. Orange and blue dots indicate actual values of the deflection ratio for load-bearing masonry and framed buildings, respectively, on shallow foundations. Black dots indicate greenfield-based deflection ratios

	p/E	E/G
Hogging	$a_{lbm,sh} = 1.098 * 10^{-5}$	$b_{lbm,sh} = 3.325$
	$a_{frm,sh} = 2.237 * 10^{-5}$	$b_{frm,sh} = 5.431$
Sagging	$a_{lbm,sh} = 2.501 * 10^{-6}$	$b_{lbm,sh} = 3.0871$
	$a_{frm,sh} = 1.278 * 10^{-5}$	$b_{frm,sh} = 3.762$

TABLE 2 Coefficients obtained by fitting the actual deflection ratios for load-bearing masonry (lbm) and framed (frm) buildings on shallow foundations (sh), distinguishing between hogging and sagging

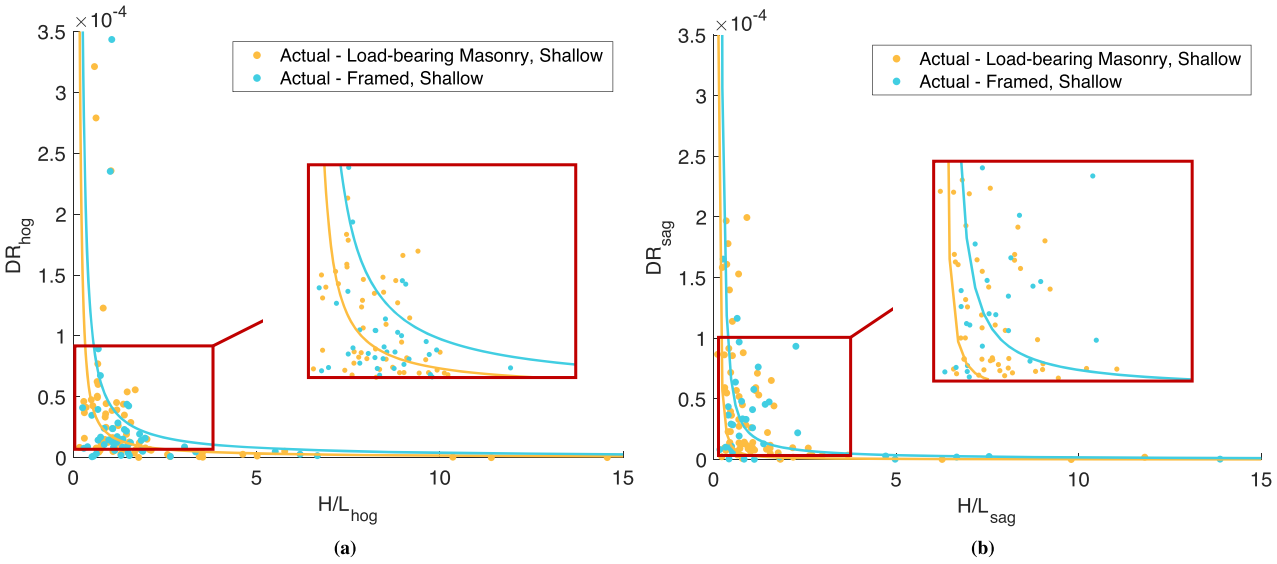

FIGURE 15 Deflection ratio DR against the building aspect ratio H/L (a) in hogging and (b) in sagging. Orange and blue dots indicate actual values of the deflection ratio for load-bearing masonry and framed buildings, respectively, on shallow foundations. The lines indicate the fitting curves, which vary according to the coefficients $a = p/E$ and $b = E/G$

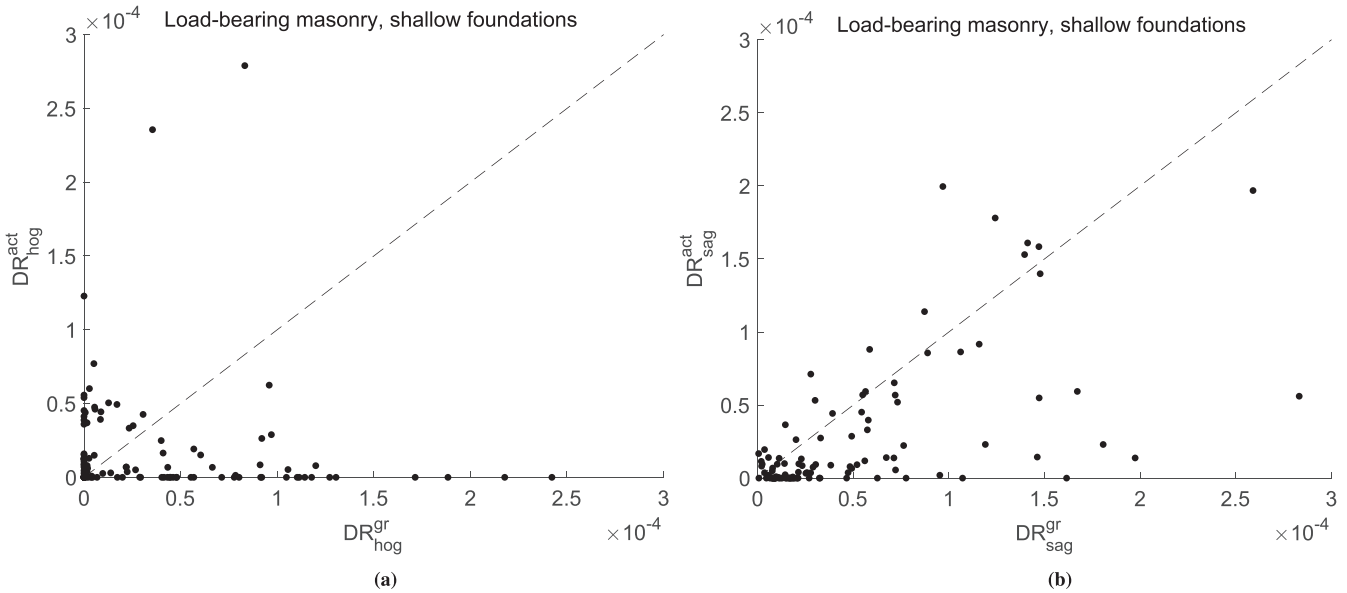

FIGURE 16 Actual deflection ratio, DR^{act}, versus greenfield-based deflection ratio, DR^{gr}, for load-bearing masonry buildings on shallow foundations in (a) hogging and (b) sagging

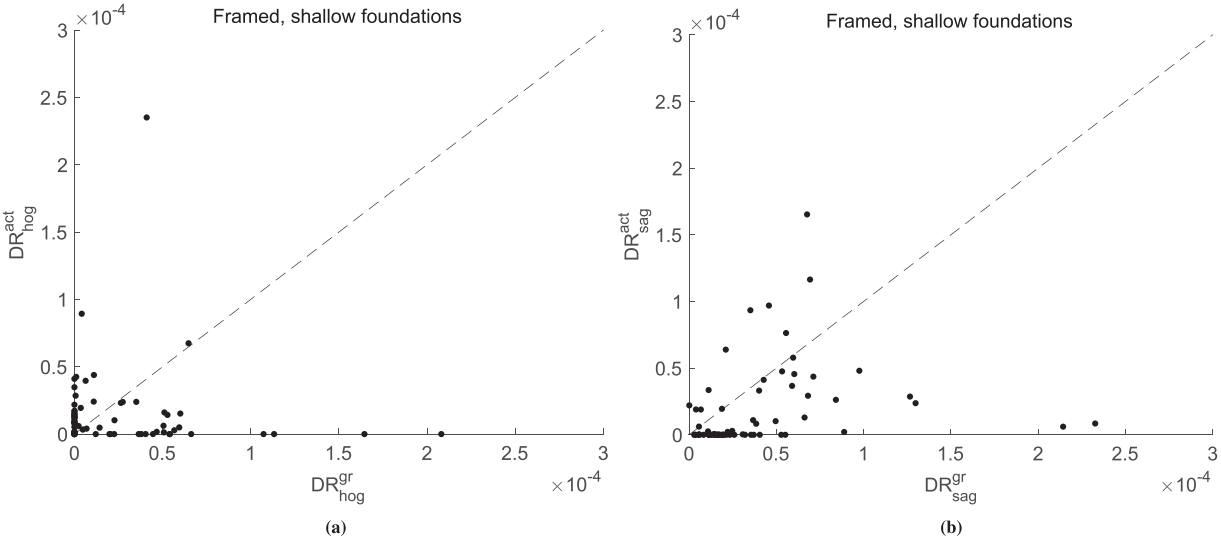

FIGURE 17 Actual deflection ratio, DR^{act}, versus greenfield-based deflection ratio, DR^{gr}, for framed buildings on shallow foundations in (a) hogging and (b) sagging

load-bearing masonry and framed buildings, respectively, on piled foundations. It can be observed that the actual deflection ratio is not always lower than the corresponding greenfield estimation. This means that greenfield predictions are not consistently conservative, and the effect of buildings should be carefully evaluated in damage assessment procedure. The effect is more evident in hogging than in sagging. This behaviour can be observed for three of the four categories, i.e. load-bearing masonry buildings on shallow foundations, framed buildings on shallow foundations and framed buildings on piled foundations, while the load-bearing masonry buildings on piled foundations are not enough to enable the observation of a trend. About 40% of load-bearing masonry buildings on shallow foundations, 49% of framed buildings on shallow foundations and 64% of framed buildings on piled foundations showed deflection ratios higher than the corresponding greenfield prediction, when the hogging deformation mode is analysed. About 20% of load-bearing masonry buildings on shallow foundations, 17% of framed buildings on shallow foundations and 3% of framed buildings on piled foundations showed deflection ratios higher than the corresponding greenfield prediction in sagging.

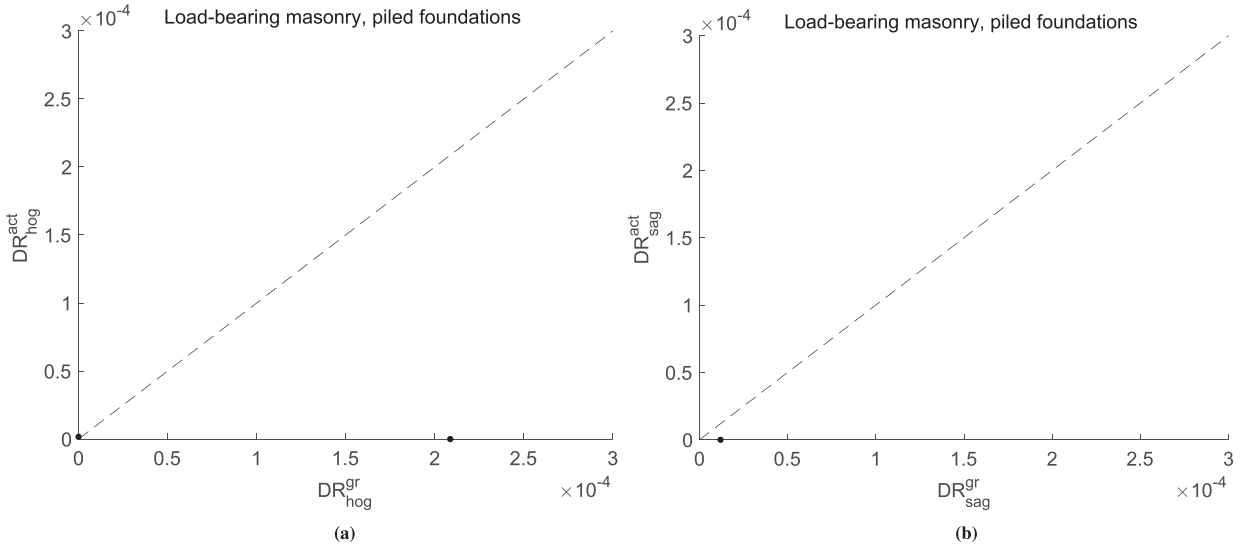

FIGURE 18 Actual deflection ratio, DR^{act}, versus greenfield-based deflection ratio, DR^{gr}, for load-bearing masonry buildings on piled foundations in (a) hogging and (b) sagging

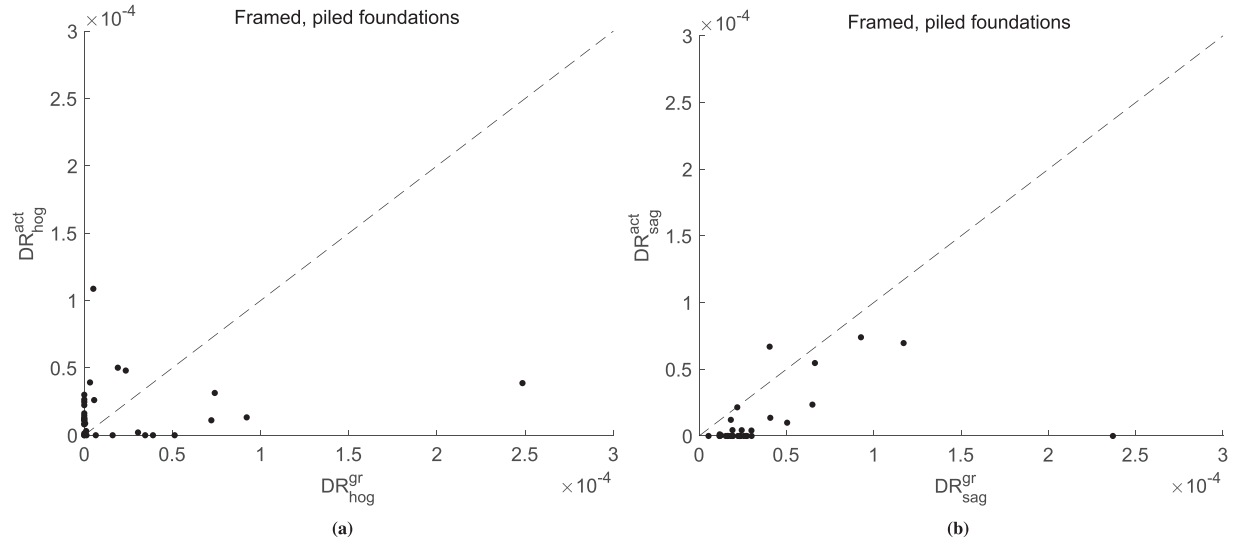

FIGURE 19 Actual deflection ratio, DR^{act}, versus greenfield-based deflection ratio, DR^{gr}, for framed buildings on piled foundations in (a) hogging and (b) sagging

We then investigated the relation of actual and greenfield deflection ratios with the building geometry, H/L, distinguishing between different structure and foundation types, and between hogging and sagging. Buildings were grouped in three different classes according to their geometry: $H/L \leq 0.5$, $0.5 < H/L \leq 2$ and $H/L > 2$. Then, for each of the following structural and foundation categories: load-bearing masonry buildings on shallow foundations; framed buildings on shallow foundations; framed buildings on piled foundations, and for each range of H/L, actual and greenfield deflection ratios were compared. Table 3 shows the number of buildings with actual deflection ratio higher than the predicted greenfield, for each structural and foundation category and in each defined range of the height-to-length ratio, when hogging or sagging deformation modes are analysed. In hogging and when $H/L \leq 2$, the greenfield underestimates the actual prediction for more than 70% of load-bearing masonry and framed buildings on shallow foundations, and for more than 80% of framed buildings on piled foundations. In sagging, the greenfield tends to overestimate the actual prediction for most of the buildings in each structural and foundation category and in each range of H/L.

TABLE 3 Percentage number of load-bearing masonry buildings on shallow foundations (lbm,sh), framed buildings on shallow foundations (frm,sh) and framed buildings on piled foundations (frm,pl) showing actual deflection ratios (DR^{act}) higher than the corresponding greenfield (DR^{gr}), in hogging and sagging

Building category	Number of buildings ($H/L \leq 0.5$)	Number of buildings ($0.5 < H/L \leq 2$)	Number of buildings ($H/L > 2$)
$\left(DR^{act}_{hog} > DR^{gr}_{hog}\right)_{lbm,sh}$	71%	72%	9%
$\left(DR^{act}_{sag} > DR^{gr}_{sag}\right)_{lbm,sh}$	30%	32%	2%
$\left(DR^{act}_{hog} > DR^{gr}_{hog}\right)_{frm,sh}$	100%	72%	11%
$\left(DR^{act}_{sag} > DR^{gr}_{sag}\right)_{frm,sh}$	29%	32%	6%
$\left(DR^{act}_{hog} > DR^{gr}_{hog}\right)_{frm,pl}$	80%	87%	31%
$\left(DR^{act}_{sag} > DR^{gr}_{sag}\right)_{frm,pl}$	0%	12%	0%

Note: Buildings in each category are grouped according to their height-to-length ratio H/L.

It should be noted that all of these observed trends are dependent upon the assumption that the PS points can be adequately fit with the modified Gaussian curve described by Equation (10). While this assumption has been previously adopted,[36] its validity may vary depending on the quality of the data for a given building. Further investigation of the effects of curve fitting of the InSAR data is the subject of ongoing work.

6 | CONCLUSION

We presented a semi-automated methodology based on the integration of PS-InSAR monitoring data and damage assessment procedures for the identification of tunnelling-induced damage to buildings. The methodology was tested on a 25-km^2 area between Paddington and Liverpool Stre et along the Crossrail twin tunnel route in London. We used descending COSMO-SkyMed PS-InSAR data acquired between 2011 and 2015 to retrieve the building displacements over the monitored area. The COSMO-SkyMed dataset provided 9146 monitoring points (PSs) on the buildings along the alignment, enabling the tunnelling-induced settlement to be reconstructed for 858 buildings. Each settlement profile was used to retrieve critical strains for the corresponding building. On the basis of the retrieved strain a category of damage was assigned to each structure and used to generate damage maps. A comparison between the PS-InSAR-based assessment and the traditional greenfield-based assessment confirmed that the greenfield assumption overestimates the damage prediction, providing a number of observations larger than any field of experimental campaign up to date. The analysed area consists of buildings built in diverse historical periods, exhibiting different structural typologies and types of foundation. This offered the possibility to investigate the structural response to tunnelling-induced settlement for different classes of buildings. The following conclusions can be drawn:

- InSAR monitoring techniques can provide a dense amount of building measurements which is not available through ground-based monitoring systems traditionally used in underground construction projects;
- the integration of InSAR measurements and building information at city-scale level provided an unprecedented amount of high quality field data on the building response to tunnelling;
- the comparison between damage indicators retrieved through InSAR-based displacements and the conventional greenfield approach quantifies the greenfield-based overestimation of building damage, giving a measure of the practical benefit of the developed approach;
- a comparison between greenfield and InSAR-derived settlement profiles showed that the presence of buildings tend to flatten the settlement curves, but not always reduce the magnitude of vertical settlements. This was observed for buildings positioned asymmetrically to the tunnels and with one end above the tunnel axis, which led to an induced vertical displacement larger than the corresponding greenfield.

- PS-InSAR-based deflection ratios reflected a different behaviour for load-bearing masonry and framed buildings on shallow foundations. Specifically, framed buildings showed a reduced stiffness and higher deflection ratios. This was more evident in hogging than in sagging;
- a comparison between actual and greenfield deflection ratios for different classes of structure and foundation showed that the greenfield overestimation is larger in hogging than in sagging;
- actual and greenfield deflection ratios were analysed in relation with the building height-to-length ratio H/L for different classes of structure and foundation. In hogging, the greenfield-based assessment underestimated the actual deformation for more than 70% of load-bearing and framed buildings on shallow foundations with $H/L < 2$, for more than 80% of framed buildings on piled foundations with $H/L < 2$, and for more than 30% of framed buildings on piled foundations with $H/L > 2$. In sagging, the greenfield-based assessment overestimated the actual deformation for most of the buildings in each structural and foundation category and in every range of H/L.

The presented methodology enables the identification of vulnerable buildings along the tunnel track, with an excellent compromise between accuracy and economical constraints. This work can positively impact the construction industry, enabling to improve traditional damage assessment strategies and to complement ground-based monitoring systems. Thanks to the large amount of building measurements available with InSAR, this methodology can be used to advance the knowledge on the soil–structure interaction and improve prediction procedures for future excavation projects.

ACKNOWLEDGEMENTS

We thank the Italian Space Agency (ASI) for providing COSMO-SkyMed data for this project: original COSMO-SkyMed product ASI Agenzia Spaziale Italiana (2011–2016). V. Macchiarulo was supported by a PhD scholarship granted by Sue and Roger Whorrod and the Alumni programme of the University of Bath. Part of this research was carried out when P. Milillo was at the Jet Propulsion Laboratory, California Institute of Technology, under a contract with the National Aeronautics and Space Administration.

CONFLICT OF INTEREST

The authors declare no potential conflict of interests.

DATA AVAILABILITY STATEMENT

The data that support the findings of this study are openly available in 4TU. ResearchData at http://doi.org/10.4121/14561934.

ORCID

Valentina Macchiarulo https://orcid.org/0000-0002-0585-0560
Pietro Milillo https://orcid.org/0000-0002-1171-3976
Matthew J. DeJong https://orcid.org/0000-0002-6195-839X
Giorgia Giardina https://orcid.org/0000-0002-5996-5830

REFERENCES

1. Broere W. Urban underground space: solving the problems of today's cities. *Tunn Undergr Space Technol*. 2015;55:245-248.
2. Azzali S. Public transport in the Gulf Region: is the development of a BRT system a viable option for Doha? *J Sustain Dev*. 2017;10:234-240.
3. Enright T. *The Making of Grand Paris: Metropolitan Urbanism in the twenty-First Century*: Cambridge, Massachusetts, USA: MIT Press; 2016.
4. Henn L, Sloan K, Douglas N. European case study on the financing of high speed rail. In: Proceedings of Australasian Transport Research Forum (ATRF). Brisbane, Queensland, Australia; 2013:2-4.
5. Kaliampakos D, Benardos A, Mavrikos A. A review on the economics of underground space utilization. *Tunn Undergr Space Technol*. 2016;55:236-244.
6. Chodorowski A, Ingram P, Black M. Crossrail project: the impact of 4–18 Bishop's Bridge Road on the new Elizabeth line, London, UK. *Proc Inst Civil Eng-Geotech Eng*. 2020;174(1):83-90.
7. Lazarus D, Jung H-I. Damage assessment and monitoring for buildings on the Elizabeth line. *Struct Eng: J Inst Struct Eng*. 2018;96(7):14-24.

8. Burland JB, Standing JR, Jardine FM. *Building Response to Tunnelling: Case Studies from Construction of the Jubilee Line Extension*, Vol. 1. London: Thomas Telford; 2001.
9. Torp-Petersen GE, Black MG. Geotechnical investigation and assessment of potential building damage arising from ground movements: Crossrail. *Proceedings of the Institution of Civil Engineers: Transport*. Thomas Telford Ltd; 2001:107-119.
10. González Martí J, Szabo B, Brzeski J. Use of linked monitoring systems for asset protection at Finsbury Circus during SCL tunnelling for Crossrail Station. *Crossrail Project: Infrastructure Design and Construction*: 2. London, UK: ICE Publishing; 2015:315-345.
11. Korff M, Kaalberg FJ. Monitoring dataset of deformations related to deep excavations for north–south line in Amsterdam. In: International symposium on geotechnical aspects of underground construction in soft ground CRC Press/Balkema. Leiden, the Netherlands; 2014:321-326.
12. DeJong MJ, Giardina G, Chalmers B, Lazarus D, Ashworth D, Mair RJ. Impact of the Crossrail tunnelling project on masonry buildings with shallow foundations. *Proc Inst Civil Eng-Geotech Eng*. 2019;172(5):402-416.
13. Bamler R, Hartl P. Synthetic aperture radar interferometry. *Inverse Probl*. 1998;14(4):R1.
14. Rosen PA, Hensley S, Joughin IR, Li FK, Madsen SN, Rodriguez E, Goldstein RM. Synthetic aperture radar interferometry. *Proc IEEE*. 2000;88(3):333-382.
15. Berardino P, Fornaro G, Lanari R, Sansosti E. A new algorithm for surface deformation monitoring based on small baseline differential SAR interferograms. *IEEE Trans Geosci Remote Sens*. 2002;40(11):2375-2383.
16. Ferretti A, Savio G, Barzaghi R, et al. Submillimeter accuracy of InSAR time series: experimental validation. *IEEE Trans Geosci Remote Sens*. 2007;45(5):1142-1153.
17. Fornaro G, Reale D, Verde S. Bridge thermal dilation monitoring with millimeter sensitivity via multidimensional SAR imaging. *IEEE Geosci Remote Sens Lett*. 2013;10(4):677-681.
18. González Martí J, Barruetabeña JS, Symonidou D, Brzeski J. The thinner pen paradox. *Crossrail learning legacy report*. 2017.
19. Yun S-H, Hudnut K, Owen S, et al. Rapid damage mapping for the 2015 M_w 7.8 Gorkha earthquake using synthetic aperture radar data from COSMO–SkyMed and ALOS-2 satellites. *Seismolog Res Lett*. 2015;86(6):1549-1556.
20. Milillo P, Rignot E, Rizzoli P, Scheuchl B, Mouginot J, Bueso-Bello J, Prats-Iraola P. Heterogeneous retreat and ice melt of Thwaites Glacier, West Antarctica. *Sci Adv*. 2019;5(1):eaau3433.
21. Bianchini S, Cigna F, Righini G, Proietti C, Casagli N. Landslide hotspot mapping by means of persistent scatterer interferometry. *Environ Earth Sci*. 2012;67(4):1155-1172.
22. Hilley GE, Bürgmann R, Ferretti A, Novali F, Rocca F. Dynamics of slow-moving landslides from permanent scatterer analysis. *Science*. 2004;304(5679):1952-1955.
23. Bekaert DPS, Jones CE, An K, Huang M-H. Exploiting UAVSAR for a comprehensive analysis of subsidence in the Sacramento Delta. *Remote Sens Environ*. 2019;220:124-134.
24. Tomás R, Márquez Y, Lopez-Sanchez JM, et al. Mapping ground subsidence induced by aquifer overexploitation using advanced differential SAR interferometry: Vega Media of the Segura River (SE Spain) case study. *Remote Sens Environ*. 2005;98(2-3):269-283.
25. Bürgmann R, Hilley G, Ferretti A, Novali F. Resolving vertical tectonics in the San Francisco Bay Area from permanent scatterer InSAR and GPS analysis. *Geology*. 2006;34(3):221-224.
26. Milillo P, Riel B, Minchew B, Yun SH, Simons M, Lundgren P. On the synergistic use of SAR constellations' data exploitation for earth science and natural hazard response. *IEEE J Sel Top Appl Earth Observ Remote Sens*. 2016;9(3):1095-1100.
27. Pritchard ME, Simons M. Surveying volcanic arcs with satellite radar interferometry: the central Andes, Kamchatka, and beyond. *GSA Today*. 2004;14(8):4-11.
28. Salzer JT, Milillo P, Varley N, Perissin D, Pantaleo M, Walter TR. Evaluating links between deformation, topography and surface temperature at volcanic domes: results from a multi-sensor study at Volcán de Colima, Mexico. *Earth Planet Sci Lett*. 2017;479:354-365.
29. Ferretti A, Prati C, Rocca F. Nonlinear subsidence rate estimation using permanent scatterers in differential SAR interferometry. *IEEE Trans Geosci Remote Sens*. 2000;38(5):2202-2212.
30. Ferretti A, Prati C, Rocca F. Permanent scatterers in SAR interferometry. *IEEE Trans Geosci Remote Sens*. 2001;39(1):8-20.
31. Perissin D, Ferretti A. Urban-target recognition by means of repeated spaceborne SAR images. *IEEE Trans Geosci Remote Sens*. 2007;45(12):4043-4058.
32. Bianchini S, Pratesi F, Nolesini T, Casagli N. Building deformation assessment by means of persistent scatterer interferometry analysis on a landslide-affected area: the Volterra (Italy) case study. *Remote Sens*. 2015;7(4):4678-4701.
33. Cerchiello V, Tessari G, Velterop E, Riccardi P, Defilippi M, Pasquali P. Building damage risk by modeling interferometric time series. *IEEE Geosci Remote Sens Lett*. 2017;14(4):509-513.
34. Cigna F, Del Ventisette C, Liguori V, et al. Advanced radar-interpretation of InSAR time series for mapping and characterization of geological processes. *Nat Hazards Earth Syst Sci*. 2011;11(3):865-881.
35. Drougkas A, Verstrynge E, Van Balen K, et al. Country-scale InSAR monitoring for settlement and uplift damage calculation in architectural heritage structures. *Struct Health Monit*. 2020:1475921720942120.
36. Giardina G, Milillo P, DeJong MJ, Perissin D, Milillo G. Evaluation of InSAR monitoring data for post-tunnelling settlement damage assessment. *Struct Control Health Monit*. 2019;26(2):e2285.
37. Macchiarulo V, Giardina G, Milillo P, González Martí J, Sánchez J, DeJong MJ. Settlement-induced building damage assessment using MT-InSAR data for the Crossrail case study in London. In: *International Conference on Smart Infrastructure and Construction 2019 (ICSIC) Driving Data-Informed Decision-Making*. Cambridge, UK: ICE Publishing; 2019:721-727.

38. Milillo P, Giardina G, DeJong MJ, Perissin D, Milillo G. Multi-temporal InSAR structural damage assessment: the London Crossrail case study. *Remote Sens*. 2018;10(2):287.
39. Peduto D, Nicodemo G, Maccabiani J, Ferlisi S. Multi-scale analysis of settlement-induced building damage using damage surveys and DInSAR data: a case study in the Netherlands. *Eng Geology*. 2017;218:117-133.
40. Shimoni M, Lopez J, Walstra J, et al. GEPATAR: a geotechnical based PS-InSAR toolbox for architectural conservation in Belgium. In: *2017 IEEE International Geoscience and Remote Sensing Symposium (IGARSS)*.Forth Worth, Texas, USA: IEEE; 2017:5555-5558.
41. Zhu M, Wan X, Fei B, et al. Detection of building and infrastructure instabilities by automatic spatiotemporal analysis of satellite SAR interferometry measurements. *Remote Sens*. 2018;10(11):1816.
42. Tapete D, Cigna F. Site-specific analysis of deformation patterns on archaeological heritage by satellite radar interferometry. *MRS Online Proc Library Archive*. 2012;1374:283-295.
43. DePrekel K, Bouali E, Oommen T. Monitoring the impact of groundwater pumping on infrastructure using Geographic Information System (GIS) and Persistent Scatterer Interferometry (PSI). *Infrastructures*. 2018;3(4):57.
44. Milillo P, Giardina G, Perissin D, Milillo G, Coletta A, Terranova C. Pre-collapse space geodetic observations of critical infrastructure: the Morandi Bridge, Genoa, Italy. *Remote Sens*. 2019;11(12):1403.
45. Selvakumaran S, Plank S, Geiß C, Rossi C, Middleton C. Remote monitoring to predict bridge scour failure using interferometric synthetic aperture radar (InSAR) stacking techniques. *Int J Appl Earth Observ Geoinformation*. 2018;73:463-470.
46. Di Martire D, Iglesias R, Monells D, et al. Comparison between differential SAR interferometry and ground measurements data in the displacement monitoring of the earth-dam of Conza della Campania (Italy). *Remote Sens Environ*. 2014;148:58-69.
47. Milillo P, Bürgmann R, Lundgren P, et al. Space geodetic monitoring of engineered structures: the ongoing destabilization of the Mosul dam, Iraq. *Sci Rep*. 2016;6:37408.
48. Milillo P, Perissin D, Salzer JT, et al. Monitoring dam structural health from space: insights from novel InSAR techniques and multi-parametric modeling applied to the Pertusillo dam Basilicata, Italy. *Int J Appl Earth Observ Geoinformation*. 2016;52:221-229.
49. Chang L, Dollevoet RPBJ, Hanssen RF. Nationwide railway monitoring using satellite SAR interferometry. *IEEE J Sel Top Appl Earth Observ Remote Sens*. 2016;10(2):596-604.
50. Infante D, Di Martire D, Calcaterra D, Miele P, Scotto di Santolo A, Ramondini M. Integrated Procedure for Monitoring and Assessment of Linear Infrastructures Safety (I-Pro MONALISA) affected by slope instability. *Appl Sci*. 2019;9(24):5535.
51. Bekaert DPS, Hamlington BD, Buzzanga B, Jones CE. Spaceborne synthetic aperture radar survey of subsidence in Hampton Roads, Virginia (USA). *Sci Reports*. 2017;7(1):1-9.
52. Heleno SIN, Oliveira LGS, Henriques MJ, et al. Persistent scatterers interferometry detects and measures ground subsidence in Lisbon. *Remote Sens Environ*. 2011;115(8):2152-2167.
53. Khorrami M, Alizadeh B, Ghasemi Tousi E, Shakerian M, Maghsoudi Y, Rahgozar P. How groundwater level fluctuations and geotechnical properties lead to asymmetric subsidence: a PSInSAR analysis of land deformation over a transit corridor in the Los Angeles Metropolitan Area. *Remote Sens*. 2019;11(4):377.
54. Musson RMW, Haynes M, Ferretti A. Space-based tectonic modeling in subduction areas using PSInSAR. *Seismological Res Lett*. 2004; 75(5):598-606.
55. Chen F, Lin H, Li Z, Chen Q, Zhou J. Interaction between permafrost and infrastructure along the Qinghai–Tibet Railway detected via jointly analysis of C-and L-band small baseline SAR interferometry. *Remote Sens Environ*. 2012;123:532-540.
56. Colesanti C, Mouelic SL, Bennani M, Raucoules D, Carnec C, Ferretti A. Detection of mining related ground instabilities using the permanent scatterers technique—a case study in the east of France. *Int J Remote Sens*. 2005;26(1):201-207.
57. Luo Q, Zhou G, Perissin D. Monitoring of subsidence along Jingjin inter-city railway with high-resolution TerraSAR-X MT-InSAR analysis. *Remote Sens*. 2017;9(7):717.
58. Raucoules D, Bourgine B, De Michele M, et al. Validation and intercomparison of persistent scatterers interferometry: PSIC4 project results. *J Appl Geophys*. 2009;68(3):335-347.
59. Bianchini Ciampoli L, Gagliardi V, Clementini C, Latini D, Del Frate F, Benedetto A. Transport infrastructure monitoring by InSAR and GPR data fusion. *Surv Geophys*. 2019: 41(3):371-394.
60. Liu G, Jia H, Zhang R, et al. Exploration of subsidence estimation by persistent scatterer InSAR on time series of high resolution TerraSAR-X images. *IEEE J Sel Top Appl Earth Observ Remote Sens*. 2010;4(1):159-170.
61. Ma P, Li T, Fang C, Lin H. A tentative test for measuring the sub-millimeter settlement and uplift of a high-speed railway bridge using COSMO-SkyMed images. *ISPRS J Photogrammetry Remote Sens*. 2019;155:1-12.
62. Wang H, Chang L, Markine V. Structural health monitoring of railway transition zones using satellite radar data. *Sensors*. 2018;18 (2):413.
63. Gheorghe M, Armaş I, Dumitru P, Călin A, Bădescu O, Necsoiu M. Monitoring subway construction using Sentinel-1 data: a case study in Bucharest, Romania. *Int J Remote Sens*. 2020;41(7):2644-2663.
64. González Martí J, Nevard S, Sanchez J. The use of InSAR (Interferometric Synthetic Aperture Radar) to complement control of construction and protect third party assets. *Crossrail Learn Legacy Report*. London, UK: Crossrail Ltd; 2017.
65. Perissin D, Wang T. Time-series InSAR applications over urban areas in China. *IEEE J Sel Top Appl Earth Observ Remote Sens*. 2011; 4(1):92-100.
66. Roccheggiani M, Piacentini D, Tirincanti E, Perissin D, Menichetti M. Detection and monitoring of tunneling induced ground movements using Sentinel-1 SAR Interferometry. *Remote Sens*. 2019;11(6):639.

67. Wang H, Feng G, Xu B, et al. Deriving spatio-temporal development of ground subsidence due to subway construction and operation in delta regions with PS-InSAR data: A case study in Guangzhou, China. *Remote Sens*. 2017;9(10):1004.
68. Reinders KJ, Hanssen RF, van Leijen FJ, Korff M. Augmented satellite InSAR for assessing short-term and long-term surface deformation due to shield tunnelling. *Tunn Undergr Space Technol*. 2021;101:103745.
69. King M, Thomas I, Stenning A. Crossrail project: machine-driven tunnels on the Elizabeth line, London. *Proceedings of the Institution of Civil Engineers*, Vol. 170. Thomas Telford Ltd; 2017:31-38.
70. Burland JB, Standing JR, Jardine PM. Assessing the risk of building damage due to tunnelling-lessons from the Jubilee Line Extension, London. In: Geotechnical Engineering: Meeting Society'S Needs: Proceedings of the Fourteenth Southeast Asian Geotechnical Conference, Vol. 1. Hong Kong: CRC Press; 2001:17.
71. Rankin WJ. Ground movements resulting from urban tunnelling: predictions and effects. *Geolog Soc London, Eng Geology Special Publ*. 1988;5(1):79-92.
72. Mair RJ, Taylor RN, Burland JB. Prediction of ground movements and assessment of risk of building damage due to bored tunnelling. In: *Fourth International Symposium of International Conference of Geotechnical Aspects of on Underground Construction in Soft Ground*. Rotterdam, Netherlands: AA Balkema; 1996:713-718.
73. Peck RB. Deep excavations and tunneling in soft ground. *Proc 7th ICSMFE, 1969*. 1969;1969:225-290.
74. O'Reilly MP, New BM. Settlements above tunnels in the United Kingdom—their magnitude and prediction; 1982.
75. Attewell PB, Yeates J, Selby AR. Soil movements induced by tunnelling and their effects on pipelines and structures; 1986.
76. Papastamos G, Stiros S, Saltogianni V, Kontogianni V. 3-D strong tilting observed in tall, isolated brick chimneys during the excavation of the Athens Metro. *Appl Geomatics*. 2015;7(2):115-121.
77. Burland JB, Wroth CP. Settlement of buildings and associated damage. In: SOA Review, Conf. Settlement of Structures. cambridge; 1974:651-654.
78. Boscardin MD, Cording EJ. Building response to excavation-induced settlement. *J Geotechn Eng*. 1989;115(1):1-21.
79. Potts DM, Addenbrooke TI. A structure's influence on tunnelling-induced ground movements. *Proc Inst Civil Engineers-Geotechn Eng*. 1997;125(2):109-125.
80. Liu G, Houlsby GT, Augarde CE. 2-dimensional analysis of settlement damage to masonry buildings caused by tunnelling. *Struct Eng*. 2000;79(1):19-25.
81. Franzius JN, Potts DM, Burland JB. The response of surface structures to tunnel construction. *Proc Inst Civil Engineers-Geotechn Eng*. 2006;159(1):3-17.
82. Amorosi A, Boldini D, De Felice G, Malena M, Sebastianelli M. Tunnelling-induced deformation and damage on historical masonry structures. *Géotechnique*. 2014;64(2):118-130.
83. Giardina G, DeJong MJ, Mair RJ. Interaction between surface structures and tunnelling in sand: centrifuge and computational modelling. *Tunnell Undergr Space Technol*. 2015;50:465-478.
84. Taylor R, Yip D, Jardine FM. Centrifuge modelling on the effect of a structure on tunnelling-induced ground movements. In: *Response of Buildings to Excavation-induced Ground Movements Conference. London, UK: CIRIA*; 2001:601-611.
85. Caporaletti P, Burghignoli A, Taylor RN. Centrifuge study of tunnel movements and their interaction with structures. In: *Geotechnical Aspects of Underground Construction in Soft Ground: Proceedings of the 5th International Symposium TC28*. Amsterdam, The Netherlands: *CRC* Press, London, UK; 2005:99-106.
86. Ritter S, De Jong MJ, Giardina G, Mair RJ. Influence of building characteristics on tunnelling-induced ground movements. *Geotechnique*. 2017;67(10):926-937.
87. Ritter S, Giardina G, DeJong MJ, Mair RJ. Centrifuge modelling of building response to tunnel excavation. *Int J Phys Modell Geotechnics*. 2017;18(3):146-161.
88. Burland JB, Mair RJ, Standing JR. Ground performance and building response due to tunnelling. In: *Advances in Geotechnical Engineering: The Skempton Conference: Proceedings of a Three Day Conference on Advances in Geotechnical Engineering, Organised by the Institution of Civil Engineers and Held at the Royal Geographical Society*. London, UK: Thomas Telford Publishing; 2004:291-342.
89. Farrell RP. Tunnelling in sands and the response of buildings. *PhD thesis*: University of Cambridge; 2011.
90. Mair R. Tunnelling and deep excavations: Ground movements and their effects. In: *Proceedings of the 15th European Conference on Soil Mechanics and Geotechnical Engineering–Geotechnics of Hard Soils–Weak Rocks (Part 4)*. Athens, Greece: IOS Press; 2013:39-70.
91. Gabriel AK, Goldstein RM, Zebker HA. Mapping small elevation changes over large areas: differential radar interferometry. *J Geophys Res Solid Earth*. 1989;94(B7):9183-9191.
92. Massonnet D, Feigl KL. Radar interferometry and its application to changes in the Earth's surface. *Rev Geophys*. 1998;36(4):441-500.
93. Crosetto M, Crippa B, Biescas E, Monserrat O, Agudo M. State of the art of land deformation monitoring using differential SAR interferometry. In: *ISPRS Hannover Workshop*. Hannover, Germany; 2005:17-20.
94. DDCMS. Principles of Selection for Listed Buildings. *Planning Requirement Document*, Department for Digital, Culture, Media & Sport, Government Digital Service. London, UK; 2010.
95. Perissin D, Wang Z, Wang T. The SARPROZ InSAR tool for urban subsidence/manmade structure stability monitoring in China. In: *Proceedings of the ISRSE*. Sidney, Australia; 2011:1015.
96. Crossrail. Phase 2 generic building damage assessment report—Drive X Running Tunnels; 2011.
97. Fuhrmann T, Garthwaite MC. Resolving three-dimensional surface motion with InSAR: constraints from multi-geometry data fusion. *Remote Sens*. 2019;11(3):241.

98. Timoshenko S. *Strength of Materials, Part I*. New York, NY: D Van Nostrand Company, Inc; 1957:19.
99. Summerson J. The Victorian rebuilding of the City of London. *London J*. 1977;3(2):163-185.
100. Crossrail. D12 ground settlement—Crossrail information paper; 2008.
101. Burland JB, Broms BB, De Mello VFB. Behaviour of foundations and structures; 1977.
102. Burland JB, Standing JR, Jardine FM. *Building response to tunnelling: case studies from construction of the Jubilee Line Extension, London*, Vol. 2. London, UK: Thomas Telford; 2001.
103. Netzel HD. Building response due to ground movements. *PhD thesis*: Delft University of Technology, TU Delft; 2009.
104. Kontogianni V, Stiros SC. Ground loss and static soil–structure interaction during urban tunnel excavation: evidence from the excavation of the Athens Metro. *Infrastructures*. 2020;5(8):64.

How to cite this article: Macchiarulo V, Milillo P, DeJong MJ, González Martí J, Sánchez J, Giardina G. Integrated InSAR monitoring and structural assessment of tunnelling-induced building deformations. *Struct Control Health Monit*. 2021;28:e2781. https://doi.org/10.1002/stc.2781